Iron deficiency drives metabolic adaptation of red pulp macrophages via FPN-SYK signaling and BCAA catabolism to enhance erythrophagocytosis

Pratik Kumar Mandal[1#], Raghunandan Mahadeva[1#], Komal Chouhan[1#], Patryk Slusarczyk[1#], Gabriela Zurawska[1], Marta Niklewicz[1], Matylda Macias[1], Aleksandra Szybińska[1], Aneta Jończy[1], Zhaoyuan Liu[2], Florent Ginhoux[3], Małgorzata Lenartowicz[4], Wojciech Pokrzywa[1], Elizabeta Nemeth[5] and Katarzyna Mleczko-Sanecka[1#]

1 International Institute of Molecular and Cell Biology in Warsaw, Poland.

2 Shanghai Institute of Immunology, Department of Immunology and Microbiology, Shanghai Jiao Tong University School of Medicine, Shanghai 200025, China.

3 Shanghai Institute of Immunology, Department of Immunology and Microbiology, Shanghai Jiao Tong University School of Medicine, Shanghai 200025, China; Singapore Immunology Network, Agency for Science, Technology and Research, Singapore 138648, Singapore; Translational Immunology Institute, SingHealth Duke-NUS Academic Medical Centre, Singapore, Singapore.

4 Laboratory of Genetics and Evolution, Institute of Zoology and Biomedical Research, Jagiellonian University, Cracow, Poland.

5 David Geffen School of Medicine at UCLA, Los Angeles, California, United States.

# - equal contribution

To whom correspondence may be addressed: Katarzyna Mleczko-Sanecka, International Institute of Molecular and Cell Biology in Warsaw, 4 Ks. Trojdena Street, 02-109 Warsaw, Poland, E-mail: kmsanecka@iimcb.gov.pl

ABSTRACT

Iron deficiency is the most common nutritional disorder worldwide, yet the mechanisms by which individual cell types adjust to iron scarcity remain unclear. Splenic red pulp macrophages (RPMs) are the key cell type for maintenance of systemic iron homeostasis. They manage exceptionally high iron flux by recycling aged red blood cells (RBCs) through erythrophagocytosis, a specialized form of efferocytosis. Yet, how RPMs adapt to iron deficiency is unknown. Surprisingly, we show that RPMs from mildly anemic, iron-deficient (ID) mice exhibit enhanced erythrophagocytic capacity. Proteomic profiling and flow cytometry revealed expansion and activation of lysosomal and mitochondrial networks, accompanied by elevated mitochondrial respiration. This metabolic rewiring and the increase in erythrophagocytosis depended on efficient branched-chain amino acid (BCAA) catabolism. These responses occurred independently of classical M2 polarization and were absent in other macrophage populations. Mechanistically, the low hepcidin-high ferroportin (FPN) axis and SYK kinase activity emerged as key drivers of this functional rewiring. Pharmacological inhibition of SYK or BCAA catabolism reversed the ID phenotype in RPMs. Together, these findings highlight a unique metabolic reprogramming of RPMs that enhances their specialized efferocytic functions during systemic iron scarcity.

INTRODUCTION

Efficient clearance of apoptotic cells, termed efferocytosis, is fundamental to tissue homeostasis and the prevention of inflammation by averting the release of potentially damaging intracellular components into the surrounding microenvironment[1–4]. Macrophages, the primary phagocytes responsible for efferocytosis, undergo profound metabolic reprogramming to sustain this process. Metabolite-driven receptor activation (e.g., PPARδ, LXR) promotes continual efferocytosis[5–7] coupled with enhanced glycolysis[8,9], fatty acid oxidation[10], mitochondrial respiration and dynamics[11,12], and an upregulated pentose phosphate pathway[13,14]. Among amino acids, the metabolism of arginine [via arginase 1 (ARG1) and ornithine decarboxylase (ODC1)][15], methionine (leading to modulation of DNA methylation)[16], tryptophan [by indoleamine 2,3-dioxygenase 1 (IDO1)][17], and glutamine [via glutaminase-1 (GLS1)-mediated glutaminolysis][18] have well-characterized roles in regulating macrophage function during efferocytosis. However, a critical gap remains in our understanding of how diverse metabolic changes are integrated and regulated across macrophage subsets and specialized efferocytic processes. In particular, very little is known about the metabolic or signaling control of erythrophagocytosis (EP), the process of clearing physiologically aged or damaged red blood cells (RBCs), which is predominantly carried out by red pulp macrophages (RPMs) in the spleen[18,19]. As RBCs constitute the body's largest iron store, their efficient removal and subsequent iron recovery are critical for supporting erythropoiesis[20,21]. Upon engulfment, RBCs are processed within phagolysosomes, releasing heme, which is catabolized by heme oxygenase 1 (HO-1) into ferrous iron (Fe^{2+}) that feeds the cellular labile iron pool (LIP). Within RPMs, iron from the LIP is either stored within ferritin or exported via ferroportin (FPN) to replenish circulating transferrin-bound iron. The iron export capacity of FPN is tightly regulated by hepcidin, a liver-derived hormone that provokes occlusion and degradation of FPN, thus ensuring systemic iron homeostasis.[20] The central role of RPMs in the maintenance of iron homeostasis is underscored by the functional attenuation in RBC clearance, accompanied by progressive splenic iron accumulation, observed in mice lacking genes essential for RPM development and during physiological aging[22–24]. Emerging evidence indicates that EP is regulated by such factors as pro-inflammatory signals[25–27], the mechanosensitive channel PIEZO1[28] via calcium (Ca^{2+}) signaling[23,28], and iron accumulation[23]. How these or other factors interact to fine-tune EP in response to varying physiological demands, particularly in states of altered iron bioavailability, remains a key unanswered question.

The critical nature of the RPM-driven recycling system takes on new significance in the face of the global burden of iron deficiency, the main cause of anemia, which impacts nearly 2 billion people (approximately 30% of the population)[29–32]. According to the 2021 Global Burden of Disease study, anemia ranks as the third leading contributor to years lived with disability worldwide, and, despite its multifactorial origins, dietary iron deficiency remains the primary cause.[31,33] Critically, the prevalence of iron deficiency itself significantly exceeds that of clinically diagnosed anemia and represents a crucial intersection between cellular iron metabolism and public health outcomes, particularly in resource-constrained developing regions[34–37]. Yet, the specific cellular vulnerabilities and the molecular mechanisms orchestrating adaptation to iron deficiency, including those operating within iron-recycling splenic RPMs, remain poorly defined.

Here, we demonstrate that RPMs in iron-deficient (ID) mice exhibit enhanced EP, and we explore how this functional adjustment is regulated by cellular signaling and metabolic rewiring. We reveal that the hepcidin-FPN axis, via regulating Ca^{2+} and spleen tyrosine kinase (SYK) signaling, enhances the EP capacity of RPMs together with their mitochondrial respiration to optimize iron recycling during iron deficiency. Furthermore, we show that RPMs uniquely rely on efficient catabolism of branched-chain amino acids (BCAAs), rich in RBCs, to enhance their EP capacity, and that this metabolic requirement remains under the control of high FPN and SYK. In sum, our findings highlight novel signaling and metabolite-driven mechanisms that shape the functional plasticity of RPMs during limited iron supplies. These insights not only deepen our understanding of RPM biology but may also inform how other macrophage populations adapt to metabolic stress or iron fluctuations in diverse physiological and pathological contexts.

RESULTS

Nutritional iron deficiency increases the EP capacity of RPMs

To investigate the impact of low systemic iron availability on EP and, more broadly, the iron-recycling capacity of RPMs, we employed a murine model of nutritional iron deficiency. To this end, four-week-old female mice were subjected to either an ID diet (<5 ppm iron) or an iron-balanced (IB) control diet (200 ppm iron) for five weeks. Dietary iron restriction resulted in significantly decreased splenic (Figure 1A) and hepatic (Figure 1B) non-heme iron concentrations in the ID group compared to the IB group, confirmed by reduced iron deposition within the splenic red pulp via Perl's staining (Figure S1A). A subtle but significant reduction in cardiac (Figure S1B)

61 non-heme iron was also observed in the ID group, while muscle (Figure S1C) tissue iron content
62 remained unaffected. These data suggested a tissue-specific response to dietary iron restriction,
63 with the spleen and the liver, the organs for iron recycling and storage, being the most affected.
64 Consistent with limited iron delivery, transferrin saturation (Figure 1C) was markedly reduced in
65 ID mice, leading to mild microcytic hypochromic anemia (Figure 1D, S1D, and S1E), which
66 hallmarks iron deficiency. Expectedly, ID mice displayed compensatory mechanisms manifested
67 by splenic stress erythropoiesis, as evidenced by elevated serum erythropoietin (EPO) (Figure S1F)
68 and increased percentage of splenic, but not bone marrow, $CD71^{+}/TER119^{+}$ progenitor cells
69 (Figure 1E and S1G).

70 Next, we aimed to precisely characterize cell-intrinsic iron parameters of RPMs in response to iron-
71 restricted feeding. Consistent with the drop in serum levels of the iron-regulatory hormone hepcidin
72 (Figure 1F), FPN expression in RPMs, assessed by immunofluorescence and flow cytometry
73 (Figure 1G and 1H), was significantly elevated in ID mice. In agreement with boosted iron-export
74 capacity, a marked decrease in total iron content was observed in the magnetically sorted RPMs of
75 ID mice (Figure 1I), along with reduced protein expression of both L- and H-ferritin (FTL and
76 FTH1; Figure 1J and 1K), indicating depletion of intracellular iron stores. Furthermore, we detected
77 upregulated levels of transferrin receptor 1 (TFR1) surface expression (Figure 1L), implying a
78 cellular response to iron deficiency. However, paradoxically, despite enhanced iron export, RPMs
79 in ID mice unexpectedly displayed a mild but significant elevation of LIP, as assessed using the
80 Fe^{2+}-specific fluorescent probe FerroOrange (Figure 1M). Consistent with this finding, we also
81 detected mildly elevated reactive oxygen species (ROS) levels in RPMs of ID versus IB mice
82 (Figure 1N).

83 Intrigued by the increased LIP in RPMs of ID mice, we investigated the capacity of EP, the major
84 route for RPM iron acquisition. To this end, we transfused mice with PKH67-labeled RBCs.
85 Strikingly, flow cytometry analysis revealed significantly enhanced phagocytosis of temperature-
86 stressed RBCs (sRBC) by RPMs from ID compared to IB mice, a phenomenon not observed for
87 non-stressed fresh RBCs that were engulfed at comparably negligible levels (Figure 1O). In
88 addition, we evaluated EP capacity across other myeloid populations, including Kupffer cells (KCs)
89 in the liver, macrophages in the bone marrow, and circulating monocytes (Figure 1O). Among
90 these, only KCs showed a statistically significant, albeit modest, increase in EP capacity in iron-
91 restricted mice. Previous work has shown that splenic red pulp sinuses trap aged RBCs, leading to

92 partial hemolysis and subsequent phagocytosis of membrane remnants (RBC ghosts) by RPMs[38].
93 To distinguish between the clearance of intact sRBCs and RBC ghosts in our model, we
94 intravenously injected mice with sRBCs ubiquitously expressing GFP and stained them with
95 PKH26 membrane dye. Consistent with our prior results, RPMs from ID mice exhibited increased
96 EP of GFP^+ $PKH26^+$ and GFP-PKH26+ sRBCs compared to control IB animals, confirming their
97 enhanced capability for the uptake of both intact RBCs and RBC ghosts (Figure 1P). Likewise,
98 splenic clearance of transfused GFP-positive sRBCs was accelerated in ID mice compared to IB
99 controls (Figure 1Q), further supporting enhanced sRBC removal by RPMs within the low-iron
100 splenic microenvironment. To validate sRBC transfusion assay results, we next assessed
101 intracellular levels of the erythrocyte marker TER119 in RPMs as a measure of endogenous EP
102 capacity[23,39], confirming its elevation in ID mice (Figure 1R). Finally, we verified whether
103 increased EP in low-iron mice is solely driven by macrophage-intrinsic mechanisms or could result
104 from erythrocyte-derived signals. RBC lifespan remained comparable between IB and ID mice
105 (Figure 1S), suggesting that iron restriction did not compromise RBC integrity. Next, exposure of
106 the apoptotic cell marker phosphatidylserine in splenic RBCs was not enhanced in ID compared to
107 IB mice (Figure 1T). Finally, using a co-culture assay of magnetically isolated splenic and
108 circulating RBCs with primary macrophages, we found that while aged splenic RBCs are
109 preferentially sequestered compared to circulating RBCs (Figure 1U), iron deficiency does not
110 increase splenic RBC susceptibility to phagocytosis (Figure 1V), implying no induction of RBC
111 "eat-me" signals by iron restriction. Taken together, we uncovered that systemic iron restriction
112 potentiates the cell-intrinsic RBC clearance capacity of RPMs, likely aimed at balancing the
113 increased replenishment of the plasma iron pool by FPN-mediated export.

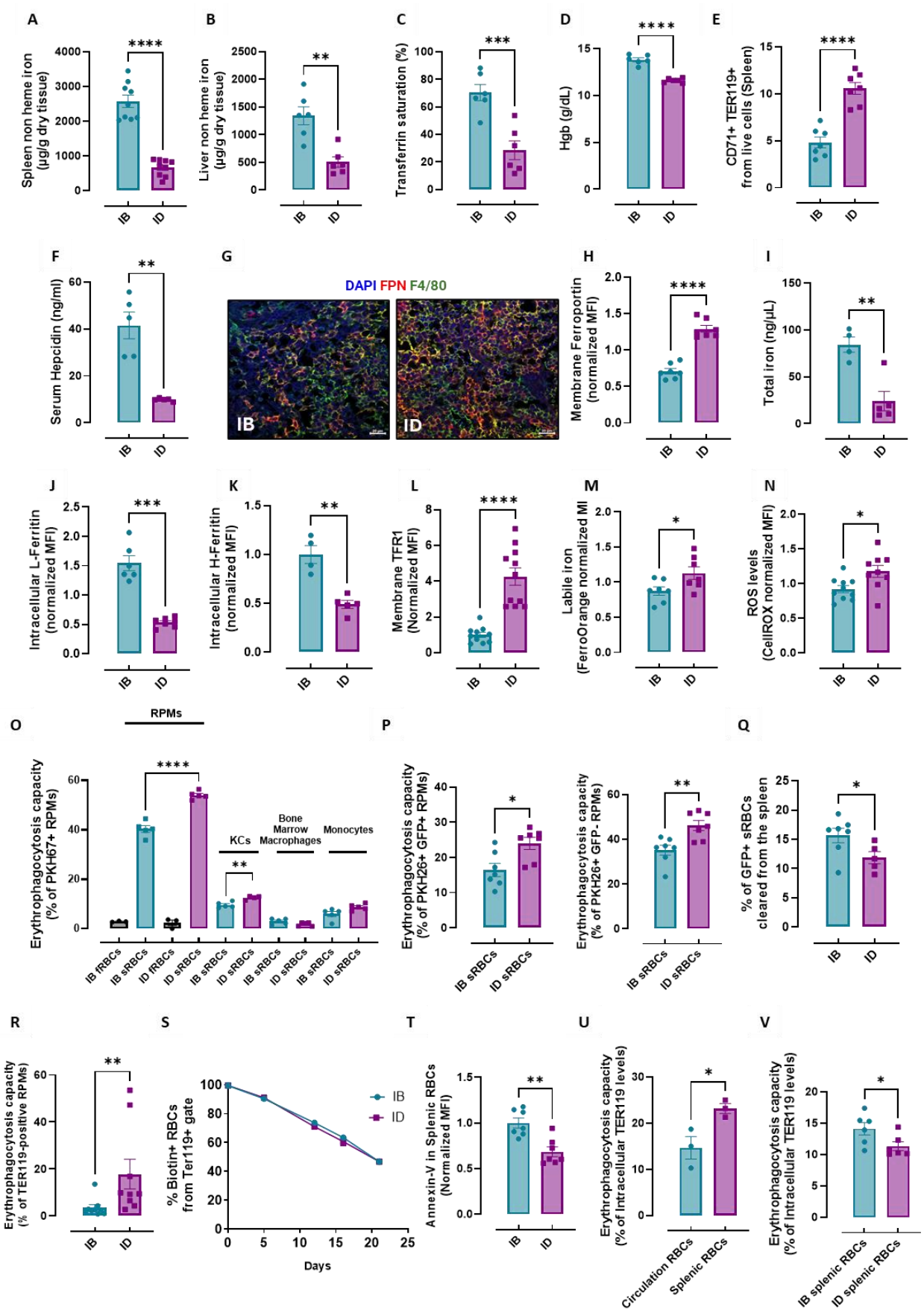
A
Spleen non heme iron (µg/g dry tissue)
B
Liver non heme iron (µg/g dry tissue)
C
Transferrin saturation (%)
D
Hgb (g/dL)
E
CD71+ TER119+ from live cells (Spleen)
F
Serum Hepcidin (ng/ml)
G
DAPI FPN F4/80
IB
ID
H
Membrane Ferroportin (normalized MFI)
I
Total iron (ng/µL)
J
Intracellular L-Ferritin (normalized MFI)
K
Intracellular H-Ferritin (normalized MFI)
L
Membrane TFR1 (Normalized MFI)
M
Labile iron (FerroOrange normalized MI
N
ROS levels (CellROX normalized MFI)
O
RPMs
KCs
Bone Marrow Macrophages
Monocytes
Erythrophagocytosis capacity (% of PKH67+ RPMs)
IB fRBCs
IB sRBCs
ID fRBCs
ID sRBCs
P
Erythrophagocytosis capacity (% of PKH26+ GFP+ RPMs)
Erythrophagocytosis capacity (% of PKH26+ GFP- RPMs)
Q
% of GFP+ sRBCs cleared from the spleen
R
Erythrophagocytosis capacity (% of TER119-positive RPMs)
S
% Biotin+ RBCs from Ter119+ gate
Days
T
Annexin-V in Splenic RBCs (Normalized MFI)
U
Erythrophagocytosis capacity (% of Intracellular TER119 levels)
Circulation RBCs
Splenic RBCs
V
IB splenic RBCs
ID splenic RBCs

114

Figure 1. Nutritional iron deficiency increases the erythrophagocytic capacity of RPMs.

(A) Spleen and (B) liver non-heme iron levels, (C) plasma transferrin saturation, and (D) blood hemoglobin (Hgb) were measured in iron-balanced (IB) and iron-deficient (ID) mice. (E) Shown is the percentage of erythroid progenitor cells (TER119+ CD71+) present in the spleen of IB and ID mice. (F) Serum hepcidin levels were measured in IB and ID mice with the Hepcidin-Murine Compete ELISA Kit. (G) Representative confocal microscopy images of FPN protein localization in the splenic red pulp of IB and ID mice. (H) Expression of FPN on the cell membrane of RPMs derived from IB and ID mice was assessed by flow cytometry. (I) The total intracellular iron content in magnetically sorted RPMs from IB and ID mice was assessed using the Iron Assay Kit. (J) Intracellular L-ferritin and (K) H-ferritin protein levels in RPMs of IB and ID mice were quantified by flow cytometry. (L) Expression of TFR1 on the cell membrane of RPMs derived from IB and ID mice was assessed by flow cytometry. (M) Cytosolic ferrous iron (Fe^{2+}) levels in RPMs of IB and ID mice were measured using the FerroOrange probe with flow cytometry. (N) The cytosolic ROS levels in RPMs of IB and ID mice were assessed by determining CellROX Deep Red fluorescence intensity with flow cytometry. (O) The erythrophagocytosis (EP) capacity in RPMs and other myeloid populations of IB and ID mice was determined using flow cytometry by measuring the percentage of cells that phagocytosed transfused PKH67-labeled RBCs. fRBCs indicate fresh RBCs, sRBCs - stressed RBCs (shown only for RPMs; in other indicated populations, fRBCs uptake was negligibly low). (P) IB and ID mice were transfused with GFP-expressing and PKH26-stained sRBCs. The percentage of RPMs positive for intact RBCs ($PKH26^{+}GFP^{+}$) and RBC ghosts ($PKH26^{+}GFP^{-}$) was determined. (Q) Flow cytometric analysis of splenic GFP-sRBC percentage in ID vs IB mice. (R) The endogenous EP capacity of RPMs derived from IB and ID mice was determined by intracellular staining of the RBC marker TER119 in RPMs and flow cytometry. (S) The RBC biotinylation lifespan assay was performed on circulating RBCs from IB and ID mice. (T) Flow cytometry assessment of phosphatidylserine exposure (Annexin V staining) in splenic RBCs of ID vs IB mice. (U) EP capacity by primary cultured macrophages (iRPM) was determined using splenic and circulating RBCs of IB mice. (V) EP capacity of iRPMs exposed to RBCs derived from the spleens of IB and ID mice. Each dot represents one mouse or an independent cell-based experiment. Each dot in the graph (S) represents n=9. Data are represented as mean ± SEM. Welch's unpaired t-test determined statistical significance between the two groups. ns $p>0.05$, *$p<0.05$, **$p<0.01$, ***$p<0.001$ and ****$p<0.0001$.

Iron deficiency drives metabolic reprogramming and enhanced lysosomal activity of RPMs via the non-canonical type of polarization

To decipher the molecular mechanisms of enhanced EP capacity in RPMs of ID mice and explore potential accompanying functional changes, we first investigated the transcriptome of FACS-isolated RPMs. Surprisingly, only 145 genes were differentially expressed between RPMs derived from ID and IB mice (Figure 2A). Bioinformatic analysis revealed significant enrichment of cell cycle regulators (e.g., *Mki67, Plk1, Plk2, Aurka, E2f7, Sgo1, Kif4, Cenpf, Bub1, Ccnb1, Ccnb2*) among genes upregulated by iron deficiency. This suggested increased pro-mitotic signaling in RPM of ID mice, which was corroborated by elevated protein levels of the proliferation marker Ki67 (Figure 2B). However, this response was not reflected by any significant change in the representation of total RPMs within $CD45^{+}$ splenic cells (Figure 2C). Likewise, using the Ms4a3Cre-RosaTdT reporter mice[40], we found no significant differences in the relative representation of residual embryonically-derived RPMs within the RPM population (Figure 2D),

157 suggesting the absence of their proliferation. The percentage of monocyte-derived RPMs also
158 remained constant at approximately 15% in both IB and ID mice (Figure 2D), implying that the EP
159 enhancement was not driven by *de novo* monocyte recruitment.

160 To further explore the adaptation of RPMs to systemic iron deficiency, we employed TMT-based
161 quantitative proteomics of magnetically-sorted F4/80-high RPMs. This analysis identified 420
162 proteins significantly more abundant and 282 decreased in RPMs of ID mice compared to IB mice
163 (Figure 2E). Confirming the quality of the proteomics analysis, we found FTH1 and FTL as the top
164 downregulated hits, and TFR1 as the most induced protein in RPMs of iron-restricted mice.
165 Consistent with this expression pattern, IRP2, a regulator of cellular iron balance, was stabilized in
166 RPMs of ID mice. In agreement with RNA-seq data, we also detected an increase in several
167 regulators of cell cycle progression, such as AURKA, AURKB, PLK1, and CDK1 in RPMs of low-
168 iron mice. Intriguingly, proteomic analysis revealed a pronounced functional rewiring of RPMs in
169 ID mice, highlighting significant post-transcriptional regulation, with far more protein-level
170 alterations and minimal overlap between transcriptomic and proteomic datasets (Figure 2F). First,
171 we observed upregulation of the phosphatidylserine-recognizing phagocytic receptors MERTK and
172 TIM4 (significant hits), and a trend towards induction of AXL and STAB2, along with the Fc
173 receptor CD16 in RPMs of ID mice, responses that were all confirmed by flow cytometry (Figure
174 2G-H, Figure S2.1A-C). Interestingly, this elevated capacity for recognizing "eat me" signals was
175 accompanied by the induction of the "don't eat me" receptor SIRPα on RPMs in ID mice (Figure
176 S2.1D), hinting at a mechanism that promotes the clearance of aged dysfunctional RBCs, sparing
177 those that are intact. Next, to gain unbiased insights into processes supporting the enhanced EP
178 capacity of RPMs in ID mice, we performed functional enrichment analyses on the differentially
179 expressed proteins. Notably, mitochondrial proteins emerged as the most significantly enriched
180 category among hits upregulated in RPMs of ID compared to IB mice (Figure 2I), including factors
181 involved in ATP synthesis (ATP5S), metabolite transport (SLC25A5, VDAC1), mitochondrial
182 protein import (SAMM50), iron-sulfur cluster assembly (SFXN2), cristae remodeling (MCCC1,
183 PMPCB), and coenzyme Q-10 biosynthesis (COQ9, COQ5). Flow cytometric analysis confirmed
184 these expanded mitochondrial functions by demonstrating a significant increase in both
185 mitochondrial membrane potential (a proxy for mitochondrial activity) (Figure 2J) and
186 mitochondrial mass (Figure 2K) in RPMs of ID mice. Consistently, RPMs of ID *versus* IB mice
187 exhibited increased uptake of fluorescently labeled glucose analog (Figure 2L) and showed a

188 significant upregulation of protein synthesis (Figure 2M), a major ATP-consuming process
189 reflective of enhanced cellular bioenergetics. Interestingly, ATP levels in FACS-sorted RPMs
190 revealed a mild depletion in ID compared to IB mice (Figure 2N), but the activation status of
191 AMPK, a key sensor of cellular energy stress, was not enhanced (Figure 2O). This suggests that
192 RPMs of ID mice did not exhibit energy deficit, but rather a state where increased ATP production
193 is insufficient to meet the high ATP demand driven by accelerated EP and protein synthesis.
194 Importantly, in contrast to RPMs, neither peritoneal macrophages (not involved in iron recycling)
195 nor iron-recycling KCs show hallmarks of metabolic rewiring in ID mice, as exemplified by
196 unaltered mitochondrial activity and mass (Figure S2.1E-H).

197 Further analysis of the proteomic data revealed another major category, encompassing proteins
198 associated with lysosomal functions, as enriched in RPMs of ID compared to IB mice (Figure 2I).
199 In total, RPMs of iron-restricted mice increased the protein levels of 25 key components of the
200 Coordinated Lysosomal Expression and Regulation (CLEAR) network, a transcriptional program
201 that drives lysosomal biogenesis and function[41] (Figure S2.2A). This included integral lysosomal
202 membrane proteins, LAMP1 and LAMP2, vacuolar ATPase subunits (ATP6V0D1, ATP6V0A1),
203 essential for lysosomal acidification, and a diverse array of lysosomal hydrolases, including
204 cathepsins B, D, and S; α-glucosidase (GAA); β-glucosidase (GBA); N-acetylglucosaminidase
205 (NAGA); and sialidase 1 (NEU1). Flow cytometric analysis confirmed elevated intracellular
206 LAMP1 levels (Figure 2P), indicating increased lysosomal mass in RPMs of ID mice. Consistent
207 with this, we observed enhanced lysosomal activity in RPMs of ID mice using a fluorescent probe
208 (Figure 2R). Further ultrastructural analysis of RPMs within splenic sections with TEM revealed
209 that while the number of regular lysosomes, autophagolysosomes, autophagosomes, and
210 peroxisomes remained unaltered between control and low-iron mice, large lysosomes were more
211 abundant in RPMs of iron-restricted mice (Figure S2.2B and S2.2C). While lysosomal size is
212 dynamic and influenced by nutrient availability, emerging evidence, for instance, from senescent
213 cells suggests that a higher proportion of enlarged lysosomes correlates with increased proteolytic
214 activity and lysosomal mass[42,43], remaining consistent with our observations. Taken together, these
215 data suggest that enhanced lysosomal function in RPMs of ID mice is coordinated with heightened
216 RBC clearance, extending the spectrum of RPMs reprogramming in iron deficiency.

217 Erythrocytic heme and iron loading, as well as systemic or cell-intrinsic iron deficiency, have been
218 shown to influence macrophage polarization, promoting either pro-inflammatory or anti-

219 inflammatory profiles, though findings have often been contradictory[44–47]. Since metabolic
220 reprogramming is closely linked to macrophage polarization, which in turn shapes the outcome of
221 infections and inflammatory diseases[48], we assessed the polarization state of RPMs from iron-
222 restricted mice. Our RNA-seq and proteomics data revealed no clear induction of either pro- or
223 anti-inflammatory mediators, alongside a mixed expression pattern of surface signals identified by
224 flow cytometry. While some markers typically associated with M1 (MHCII, CD74) and M2
225 (CD206) polarization were decreased in RPMs of ID *versus* IB mice, others, such as the pro-
226 inflammatory CD38 and the anti-inflammatory CD163, were increased (Figure S2.3). This atypical
227 combination of features suggests that augmented RBC clearance in nutritionally iron-restricted
228 mice leads to the activation state of RPMs distinct from the canonical M1 or M2 type of profile.

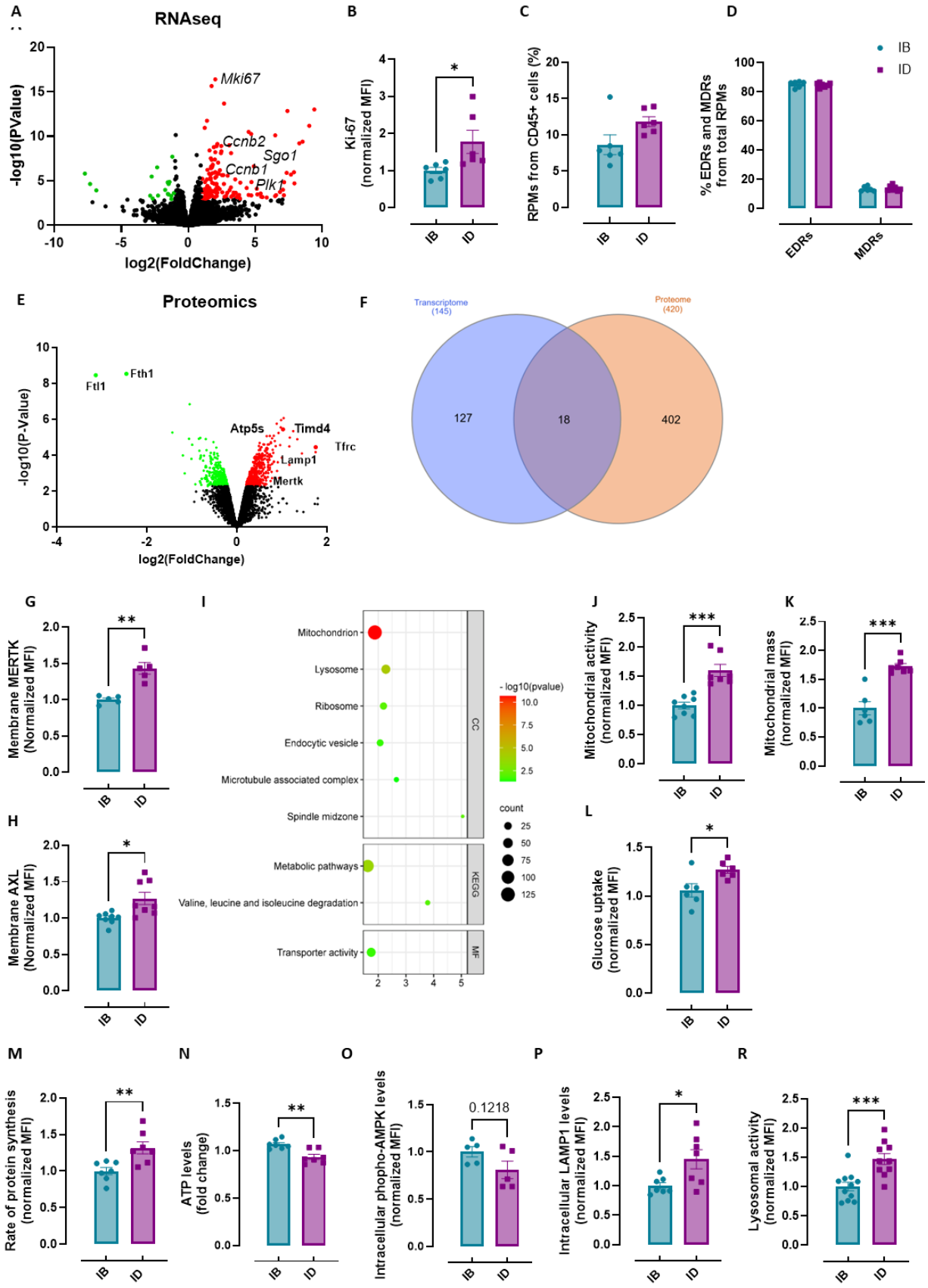
A
RNAseq
-log10(PValue)
log2(FoldChange)
Mki67
Ccnb2
Sgo1
Ccnb1
Plk1
B
Ki-67 (normalized MFI)
IB
ID
C
RPMs from CD45+ cells (%)
D
% EDRs and MDRs from total RPMs
EDRs
MDRs
E
Proteomics
-log10(P-Value)
Fth1
Ftl1
Atp5s
Timd4
Tfrc
Lamp1
Mertk
F
Transcriptome (145)
Proteome (420)
127
18
402
G
Membrane MERTK (Normalized MFI)
H
Membrane AXL (Normalized MFI)
I
Mitochondrion
Lysosome
Ribosome
Endocytic vesicle
Microtubule associated complex
Spindle midzone
Metabolic pathways
Valine, leucine and isoleucine degradation
Transporter activity
CC
KEGG
MF
- log10(pvalue)
count
J
Mitochondrial activity (normalized MFI)
K
Mitochondrial mass (normalized MFI)
L
Glucose uptake (normalized MFI)
M
Rate of protein synthesis (normalized MFI)
N
ATP levels (fold change)
O
Intracellular phopho-AMPK levels (normalized MFI)
0.1218
P
Intracellular LAMP1 levels (normalized MFI)
R
Lysosomal activity (normalized MFI)

229

Figure 2. Iron deficiency drives metabolic reprogramming and enhanced lysosomal activity of RPMs. (A) A volcano plot of differentially regulated genes identified by the RNA-Seq transcriptomic analysis in FACS-sorted RPMs derived from IB and ID mice. (B) Intracellular Ki-67 protein levels in RPMs derived from IB and ID mice were assessed by flow cytometry. (C and D) Percentage of (C) total RPMs and (D) embryonic-derived RPMs (EDRs) and monocyte-derived RPMs (MDRs) among total RPMs in IB and ID mice. (E) Volcano plot visualizing the proteomic landscape of RPMs in response to iron deficiency, depicting differentially expressed proteins in IB and ID mice. (F) Venn diagram comparing the differentially expressed genes (transcriptome) and proteins (proteome) in RPMs from ID mice. (G and H) Cell membrane expression levels of (G) MERTK and (H) AXL of RPMs in IB and ID mice were determined by using fluorescently labeled antibodies and flow cytometry. (I) Enriched functional categories among significantly increased in magnetically sorted RPMs derived from ID versus IB spleen. (J) Mitochondrial membrane potential/activity and (K) mitochondrial mass were determined in RPMs derived from IB and ID mice using TMRE probe and MitoTracker Green, respectively, with flow cytometry. (L) Quantification of glucose uptake via flow cytometry in RPMs from IB and ID mice using a fluorescent glucose analog. (M) Flow cytometric detection of newly synthesized proteins in RPMs of IB and ID mice using Click-iT Plus OPP Alexa Fluor 488 Protein Synthesis Assay. (N) Quantification of ATP levels in FACS-sorted RPMs (10,000 cells) from IB and ID mice using a chemiluminescence-based assay. (O) Intracellular phosphorylated AMPK protein levels in RPMs derived from IB and ID mice were assessed by flow cytometry. (P) Intracellular expression levels of the core lysosomal protein LAMP1 in RPMs of IB and ID mice were determined by flow cytometry. (R) Flow cytometric assessment of lysosomal activity in RPMs of IB and ID mice using the Lysosomal Intracellular Activity Assay Kit. Each dot represents one mouse. Data are represented as mean ± SEM. Welch's unpaired t-test determined statistical significance between the two groups. ns $p>0.05$, *$p<0.05$, **$p<0.01$, ***$p<0.001$ and ****$p<0.0001$.

Low hepcidin levels are critical for functional adaptations of RPMs during iron deficiency

To elucidate the mechanisms driving the enhanced EP capacity of RPMs in iron deficiency, we first investigated whether these adaptations were directly dependent on intracellular iron levels. Iron depletion *in vitro* using deferiprone (Figure 3A) or DFO[23] did not alter the RBC clearance capacity of primary BMDM macrophages cultured with hemin (iRPM). Furthermore, our *in vivo* data demonstrated that despite systemic iron deficiency, RPMs in ID mice exhibited elevated LIP (Figure 1M), likely due to their increased EP activity, indicating that iron chelation *in vitro* might not fully recapitulate the complex cellular interactions and signaling pathways present in RPMs *in vivo*. These findings suggested that factors beyond simple iron availability may be critical drivers of enhanced RPM phagocytic activity during iron deficiency. To address this possibility mechanistically, we developed an *in vitro* system using iRPMs cultured in serum derived from IB and ID mice, instead of bovine serum. This system recapitulated increased FPN and TFR1 expressions in iRPMs exposed to ID serum, without a significant change in total iron levels (Figure 3B-D). Notably, cells cultured in ID serum exhibited enhanced EP (Figure S3A), suggesting that serum-borne factor is sufficient to rewire the phagocytic capacity of iRPMs towards RBCs. We first excluded the contribution of EPO, the cytokine previously implicated as a stimulator of efferocytosis[49]. We showed that iRPMs, in contrast to BMDMs cultured without hemin, which is

270 critical to mimic the heme and iron-rich nature of RPMs, did not enhance EP even under high EPO
271 doses (Figure S3B-C). Moreover, PPARγ, a factor proposed to act downstream of EPO[49], failed to
272 alter the EP capacity of iRPMs (Figure S3C). Next, inspired by a study that revealed low hepcidin,
273 rather than iron deficiency itself, as a key driver of pro-inflammatory responses in iron-restricted
274 mice[47], we hypothesized that reduced serum hepcidin levels and enhanced FPN stabilization in
275 RPMs might play a critical role in the adaptive reprogramming of these cells. Strikingly, a 4-hour
276 treatment with the hepcidin mimetic PR73 reversed the enhanced EP phenotype in iRPMs exposed
277 to ID, but not to IB serum (Figure 3E and S3D). Likewise, we conducted live imaging of EP by
278 cultured iRPMs incubated with serum from IB and ID mice, and exposed to sRBCs labeled with a
279 dedicated pHrodo™ dye that remains non-fluorescent at neutral pH but emits fluorescence in acidic
280 environments, indicating sequestrations in phagolysosomes. In line with our flow cytometry
281 results, we observed enhanced pHrodo signal in real time in iRPMs treated with ID serum,
282 reflecting their enhanced EP capacity (Figure 3F). This boost of RBC clearance capacity was
283 significantly abrogated upon 4 hours of PR73 treatment (Figure 3F). Consistent with our *in vivo*
284 observations, ID serum induced a significant increase in both mitochondrial and lysosomal activity,
285 which was likewise abrogated by PR73 treatment (Figure S3E-H).

286 To follow these *in vitro* observations, we next administered IB and ID mice with PR73 via
287 intraperitoneal injection four hours before analysis. PR73 administration effectively reduced cell-
288 surface FPN expression and induced hypoferremia in both dietary groups (Figure 3G-H). However,
289 total RPM iron content remained unchanged in both IB and ID mice following PR73 treatment
290 (Figure 3I). PR73 administration did not reverse the increased cell surface expression of TFR1 on
291 RPMs of ID mice but instead led to its further elevation, in contrast to IB mice, where TFR1 levels
292 remained unaltered (Figure 3J). Interestingly, PR73 elicited similarly distinct effects on the LIP in
293 RPMs depending on the dietary regimen: it expectedly increased LIP levels in IB mice, but led to
294 a mild decrease in ID mice (Figure 3K). The latter pattern was, strikingly, closely reflected by the
295 pronounced reversal of the elevated EP capacity of RPMs from ID mice by PR73 injection (Figure
296 3L). Likewise, PR73 abrogated most of the other hallmarks of RPM adaptation to iron deficiency,
297 including elevated mitochondrial activity, increased glucose uptake, and heightened protein
298 synthesis (Figure 3M-O). Intriguingly, these modulating effects of PR73 were absent in IB mice.
299 Furthermore, *ex vivo* freshly isolated RPMs exhibited substantially elevated oxidative
300 phosphorylation (OXPHOS), as assessed by oxygen consumption rate measurement with Seahorse

301 (Figure 3P). Strikingly, a 4-hour preincubation of the *ex vivo* RPMs of ID mice with PR73
302 completely abolished their activated oxygen consumption (Figure 3P). Of note, these rapid effects
303 of PR73 did not include changes in the mitochondrial mass of RPMs, remaining elevated regardless
304 of PR73 injection in ID mice (Figure S3I). Similarly, lysosomal activity of RPMs of ID mice
305 remained higher than in IB mice despite PR73 supplementation, suggesting either distinct
306 regulatory mechanisms or differential kinetics governing these responses (Figure S3J). To support
307 the key role of the hepcidin-FPN axis in modulating the iron-recycling activity of RPMs, we
308 employed *Tmprss6* knockout (KO) mice, a model of iron-refractory iron deficiency anemia
309 (IRIDA)[50–52]. This model exhibits some characteristics of the nutritional ID model, including
310 reduced transferrin saturation, decreased hepatic iron stores (Figure S3K-L), and anemia. However,
311 in contrast to dietary ID conditions, *Tmprss6* KO mice display elevated hepcidin levels, and their
312 splenic iron stores remain largely unchanged[53,54], with no significant depletion observed, consistent
313 with our findings (Figure S3M). Importantly, we observed no significant difference in RPMs' EP
314 capacity between *Tmprss6* KO mice and wild-type controls (Figure 3Q). Likewise, *in vitro* cultured
315 iRPMs showed no difference in RBC clearance when exposed to serum from either *Tmprss6* KO
316 or wild-type mice (Figure 3R). In sum, these data implied that deficient hepcidin levels and FPN
317 stabilization, hallmarks of nutritional ID, are key driving factors for enhanced RPM
318 erythrophagocytic capacity and their metabolic adaptation to low systemic iron levels.

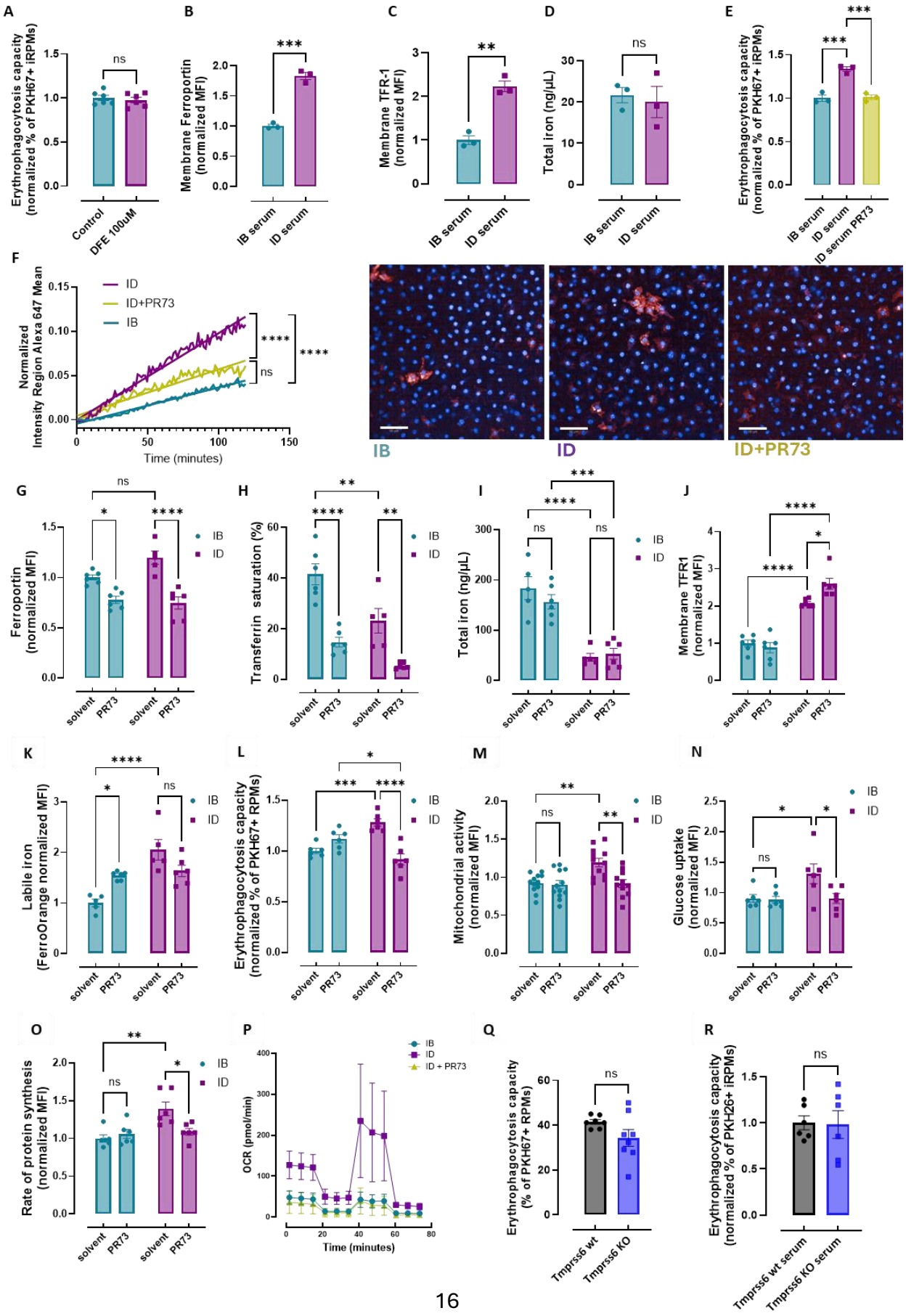
A
Erythrophagocytosis capacity (normalized % of PKH67+ iRPMs)
ns
Control
DFE 100uM
B
Membrane Ferroportin (normalized MFI)
***
IB serum
ID serum
C
Membrane TFR-1 (normalized MFI)
**
IB serum
ID serum
D
Total iron (ng/µL)
ns
IB serum
ID serum
E
Erythrophagocytosis capacity (normalized % of PKH67+ iRPMs)
***
***
IB serum
ID serum
ID serum PR73
F
Normalized Intensity Region Alexa 647 Mean
ID
ID+PR73
IB
****
****
ns
Time (minutes)
IB
ID
ID+PR73
G
Ferroportin (normalized MFI)
ns
*
****
IB
ID
solvent
PR73
H
Transferrin saturation (%)
**
****
**
I
Total iron (ng/µL)
***
****
ns
ns
J
Membrane TFR1 (normalized MFI)
****
****
*
K
Labile iron (FerroOrange normalized MFI)
****
*
ns
L
Erythrophagocytosis capacity (normalized % of PKH67+ RPMs)
*
***
****
M
Mitochondrial activity (normalized MFI)
**
ns
**
N
Glucose uptake (normalized MFI)
*
*
ns
O
Rate of protein synthesis (normalized MFI)
**
ns
*
P
OCR (pmol/min)
IB
ID
ID + PR73
Time (minutes)
Q
Erythrophagocytosis capacity (% of PKH67+ RPMs)
ns
Tmprss6 wt
Tmprss6 KO
R
Erythrophagocytosis capacity (normalized % of PKH26+ iRPMs)
ns
Tmprss6 wt serum
Tmprss6 KO serum

319

Figure 3. Low hepcidin levels are critical for functional adaptations of RPMs during iron deficiency. (A) Normalized EP capacity of PKH67-stained sRBCs by cultured iRPMs treated with an iron chelator DFE (100 μM, 18 hr). (B-C) Flow cytometry analysis of (B) surface FPN and (C) TFR1 expression on iRPMs cultured with serum from IB or ID mice. (D) The total intracellular iron content in iRPMs cultured with serum from IB or ID mice was assessed using the Iron Assay Kit. (E) The EP capacity in iRPMs cultured with serum from IB or ID mice, and serum from ID mice supplemented with the hepcidin agonist PR73 (2 μg/mL, 4 hr) determined using flow cytometry by measuring the percentage of cells that phagocytosed PKH67-labeled RBCs. (F) Time-lapse imaging of the EP progression in iRPMs, exposed to pHrodo-stained sRBCs and cultured with the serum from IB and ID mice (with and without 4-hour pretreatment with PR73). The left panel shows the quantification of the RBC fluorescent signal over time, normalized to the number of macrophages. The right panel shows example images at the endpoint of the assay. Scale bar=50 μm. (G) Flow cytometric analysis of FPN cell surface expression on RPMs from IB and ID mice following intraperitoneal administration of the hepcidin agonist PR73 (50 nmol/mouse, 4 hours). (H) Plasma transferrin saturation was determined in IB and ID mice following PR73 administration. (I) Intracellular iron content in magnetically sorted RPMs from IB and ID mice post-PR73 treatment as determined using the Iron Assay Kit. (J) Flow cytometric evaluation of TFR1 surface expression on RPMs derived from IB and ID mice post-PR73 administration. (K) Flow cytometric measurement of cytosolic ferrous iron (Fe^{2+}) levels in RPMs from IB and ID mice using FerroOrange following PR73 administration. (L) Normalized EP capacity of PKH67-sRBCs by RPMs from IB and ID mice after PR73 administration. (M) Mitochondrial activity was determined in RPMs derived from IB and ID mice using the TMRE probe post-PR73 administration, with flow cytometry. (N) Quantification of glucose uptake via flow cytometry in RPMs from IB and ID mice upon PR73 administration using a fluorescent glucose analog. (O) Flow cytometric detection of newly synthesized proteins in RPMs of IB and ID mice using Click-iT Plus OPP Alexa Fluor 488 Protein Synthesis Assay after PR73 administration. (P) Seahorse analysis of *ex vivo* RPMs from IB and ID mice, with or without 4-hour PR73 preincubation for RPMs from ID mice. (Q) Flow cytometric assessment of EP capacity in RPMs of *Tmprss6* wt and *Tmprss6* KO mice was quantified as the percentage of cells engulfing PKH67-labeled sRBCs. (R) Normalized EP capacity of PKH26 sRBCs by cultured iRPMs treated with serum from *Tmprss6* wt and *Tmprss6* KO mice was determined using flow cytometry. Each dot represents one mouse or an independent cell-based experiment. Data are represented as mean ± SEM. Welch's unpaired t-test determined statistical significance in A-D and Q-R, while two-way ANOVA with Tukey's Multiple Comparison tests was used in G-O. A one-way ANOVA test with Dunnett's or Tukey's Multiple Comparison tests was used in E. In F, the significant differences between the slopes of simple linear regression lines are shown. ns $p>0.05$, *$p<0.05$, **$p<0.01$, ***$p<0.001$ and ****$p<0.0001$.

Elevated FPN regulates RPM rewiring in ID conditions via Ca^2-dependent signaling

To further assess the role of FPN upregulation in RPM rewiring under systemic ID conditions, we used lentiviral transduction to create iRPMs with enforced FPN overexpression (FPN OE; FPN-iRPMs) and assessed whether this mimics RPM adaptation to iron deficiency. Control iRPMs were generated using an empty vector without the *Slc40a1* gene, encoding FPN (mock-iRPMs). We confirmed significant FPN elevation on the surface of FPN-iRPMs compared to control cells (Figure 4A). This further led to the elevation of TFR1 surface expression but did not significantly change the total iron levels (Figure 4B-C), thus resembling the iRPMs exposed to ID vs IB serum. Under basal conditions, we quantified the LIP in both FPN-iRPMs and mock-iRPMs, finding no significant difference (Figure 4D). In an attempt to recapitulate the mildly elevated LIP observed in RPMs of ID mice during enhanced *in vivo* EP, we next sought to mimic the splenic

364 microenvironment by continuously exposing iRPMs to sRBCs during culture. Strikingly, sRBC-
365 exposed FPN-iRPMs exhibited a significant increase in LIP compared to mock-iRPMs (Figure
366 4D), mirroring the *in vivo* RPM response (Figure 1M). Most importantly, FPN-iRPMs displayed
367 enhanced RBC clearance regardless of sRBC exposure during culture (Figure 4E), a response that
368 was efficiently reversed by suppression of FPN by a potent specific inhibitor vamifeport[55] (Figure
369 4F). These findings demonstrate that forced FPN expression and consequent increased cellular iron
370 flux, rather than overall iron content, specifically stimulate EP.

371 We next investigated in more detail the potential metabolic consequences of increased FPN
372 expression. FPN overexpression led to a significant increase in both mitochondrial activity and
373 mass compared to mock-transduced iRPMs in a manner that was likewise blocked by vamifeport
374 (Figure 4G-H). This response was reflected by a vamifeport-controlled increase in glucose uptake
375 and protein synthesis rate in FPN-overexpressing iRPMs (Figure 4I-J), suggesting a coordinated
376 metabolic adaptation. Importantly, these responses were independent of the presence of sRBCs in
377 the culture media and intracellular iRPM LIP levels (Figure S4A-D), indicating a regulatory effect
378 of FPN on mitochondrial functions that may reach beyond its role as a regulator of intracellular
379 iron status.

380 We next set out to elucidate the signaling mechanisms underlying the functional rewiring of RPMs
381 in response to increased FPN expression during systemic iron deficiency. Our previous work
382 demonstrated that age-related iron overload, likely due to low FPN expression, suppressed RPM's
383 RBC clearance capacity[23]. This phenomenon was recapitulated in iron-loaded *in vitro* iRPMs and
384 was reflected by reduced intracellular Ca^{2+} levels[23], a key regulatory signal for phagocytosis[56].
385 Extending this observation, we found a significant increase in intracellular Ca^{2+} levels within RPMs
386 of ID mice compared to IB mice (Figure 4K), mirroring the enhanced RBC clearance capacity.
387 PR73 administration reversed the elevated intracellular Ca^{2+} levels specifically in RPMs of ID
388 mice, with no effect observed in RPMs of IB mice (Figure 4L). In parallel, iRPMs exposed to ID
389 serum also displayed increased Ca^{2+} levels, a response likewise suppressed by PR73 treatment
390 (Figure 4M). This demonstrates that intracellular Ca^{2+} signaling, like phagocytic and mitochondrial
391 activities, is uniquely reprogrammed in RPMs of iron-deficient mice in a manner dependent on low
392 hepcidin/high FPN. Consistently, FPN-iRPMs exhibited increased intracellular Ca^{2+} levels
393 compared to mock-iRPMs, independent of the presence of stressed RBCs during culture and
394 cellular LIP levels, further implying the role of Ca^{2+} signaling in RPM functional rewiring driven

395 by high FPN (Figure 4N). To further examine whether enhanced Ca^{2+} signaling may support
396 increased EP in iRPMs, we employed both intracellular (BAPTA-AM) and/or extracellular (EGTA)
397 Ca^{2+} chelators in the FPN-iRPM model and iRPMs exposed to ID and IB serum (Figure 4O-P).
398 Both chelation strategies not only reduced the overall EP capacity of iRPMs but also effectively
399 suppressed the enhancement of RBC clearance in FPN-high conditions. Recent findings implied
400 that FPN may have the capacity for Ca^{2+} import[57]. To test whether FPN-mediated Ca^{2+} influx
401 directly drives their functional rewiring, we employed overexpression of the FPN variant harboring
402 a specific aspartate-to-alanine mutation (D39A), expected to disrupt the unidirectional movement
403 of Ca^{2+} into the cell while preserving Fe^{2+} transport function[54]. Interestingly, we found no
404 significant differences in the enhancement of EP or intracellular Ca^{2+} levels between iRPMs
405 overexpressing mutant D39A and wild-type FPN (Figure 4Q-R). In sum, our findings suggested
406 that FPN-mediated indirect activation of Ca^{2+} signaling contributes to enhanced phagocytic
407 capacity of RPMs.

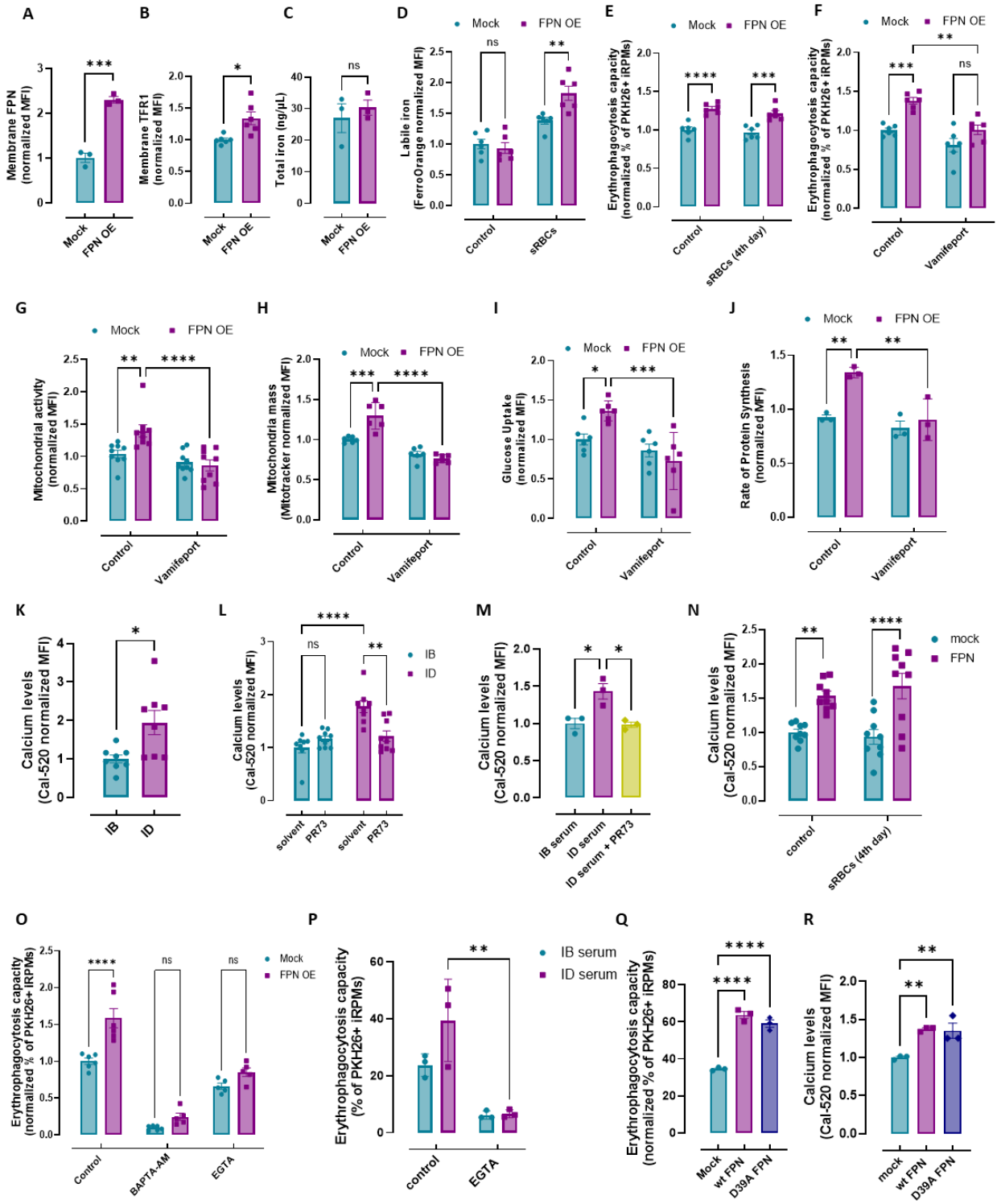

Figure 4. Elevated FPN regulates RPM rewiring in ID conditions via Ca²-dependent signaling.

(A-J) Lentiviral transduction was used to generate iRPMs overexpressing FPN (FPN OE; FPN-iRPMs) or expressing an empty vector (mock). (A-C) Flow cytometric analysis of (A) FPN and (B) TFR1 cell surface expression, and (C) intracellular iron content in mock and FPN-iRPMs determined using the Iron Assay Kit. (D) Flow cytometric measurement of cytosolic ferrous iron (Fe^{2+}) levels in mock and FPN-iRPMs with and

414 without sRBC exposure during culture. (E) Normalized EP capacity towards PKH26-sRBCs by mock and
415 FPN-iRPMs with and without sRBC exposure during culture was determined with flow cytometry. (F-J)
416 iRPMS were cultured with sRBCs and treated with vamifeport (20 μM, 15 h). (F) Normalized EP capacity
417 towards PKH26-sRBCs was determined by flow cytometry. (G) Mitochondrial activity and (H) mass were
418 determined by the TMRE and MitoTracker Green probes, respectively, and flow cytometry. (I)
419 Quantification of glucose uptake via flow cytometry using a fluorescent glucose analog. (J) Flow cytometric
420 detection of newly synthesized proteins using Click-iT Plus OPP Alexa Fluor 488 Protein Synthesis Assay
421 and flow cytometry. (K) Cytosolic calcium iron (Ca^{2+}) levels in RPMs of IB and ID mice were measured
422 using Cal-520 fluorescent probe with flow cytometry. (L) Cytosolic Ca^{2+} levels in RPMs of IB and ID mice
423 were measured with flow cytometry post-PR73 administration using Cal-520 fluorescent probe with flow
424 cytometry. (M) Cytosolic Ca^{2+} levels in iRPMs cultured with serum from IB or ID mice and serum from ID
425 mice treated with the hepcidin agonist PR73 (2 μg/mL, 4 hr) were determined using Cal-520 fluorescent
426 probe with flow cytometry. (N) Flow cytometric measurement of cytosolic Ca^{2+} levels in mock and FPN-
427 iRPMs with and without sRBC exposure using Cal-520 fluorescent probe with flow cytometry. (O)
428 Normalized EP capacity of PKH26-sRBCs by mock and FPN-iRPMs treated with an intracellular (BAPTA-
429 AM; 10 μM for 1 hour) and extracellular (EGTA; 3mM for 30 minutes) calcium chelator. (P) The EP
430 capacity in iRPMs cultured with serum from IB and ID mice, and treated with extracellular (EGTA; 3mM
431 for 30 minutes) calcium chelator, was determined using flow cytometry by measuring the percentage of
432 cells that phagocytosed PKH26-labeled sRBCs. (Q) Flow cytometric assessment of EP capacity in mock-
433 transduced iRPMs and iRPMs overexpressing wild-type FPN and FPN mutant D39A was quantified as the
434 percentage of cells engulfing PKH26-labeled RBCs. (R) Flow cytometric measurement of cytosolic Ca^{2+}
435 levels in mock, FPN, and D39A-iRPMs using Cal-520 fluorescent probe with flow cytometry. Each dot
436 represents one mouse or an independent cell-based experiment. Data are represented as mean ± SEM.
437 Welch's unpaired t-test determined statistical significance in A-C and K. Two-way ANOVA with Tukey's
438 Multiple Comparison tests was used in D-J, N, and N-P. A one-way ANOVA test with Dunnett's or Tukey's
439 Multiple Comparison tests was used in M and Q-R. ns $p>0.05$, *$p<0.05$, **$p<0.01$, ***$p<0.001$ and
440 ****$p<0.0001$.

441 **SYK kinase mediates the FPN-dependent adaptation of RPMs to ID conditions**

442 Expanding on prior knowledge, we next sought to identify the genetic mediators of Ca^{2+}-dependent
443 signaling underlying the functional rewiring of RPMs in ID mice. First, we examined the
444 involvement of PIEZO1, a mechanoreceptor identified to modulate Ca^{2+} signaling and EP in
445 RPMs[28]. Indeed, under basal conditions, treatment of iRPMs *in vitro* with the PIEZO1 activator
446 YODA1 and the inhibitor GsMTx1 mildly affected EP (Figure S5.1A-B). However, GsMTx1 did
447 not significantly affect the enhanced EP capacity observed in iRPMs exposed to ID serum (Figure
448 S5.1C). These findings excluded a major role for PIEZO1 in mediating the functional acceleration
449 of RPMs in response to iron deficiency.

450 To further dissect the Ca^{2+}-dependent signaling pathways responsible for the enhanced EP observed
451 in RPMs during iron deficiency, we performed a targeted pharmacological screen. Inhibitors of
452 CaMKK (STO-609), calmodulin-mediated signaling (W7), P2 receptor-mediated Ca^{2+} signaling
453 (Apyrase)[58], and macropinocytosis (EIPA) had no discernible impact on EP in either mock or FPN-
454 iRPMs (Figure 5A). Likewise, despite its well-established role in Ca^{2+}-dependent signaling,

455 inhibition of protein kinase C (PKC) with Bisindolylmaleimide I did not reduce EP in either mock-
456 or FPN-iRPMs (Figure 5A). However, the inhibition of the spleen tyrosine kinase (SYK), a
457 downstream effector of PKC-dependent signaling, with piceatannol completely abolished the
458 increased EP in FPN-iRPMs *versus* mock-transduced iRPMs (Figure 5A). To mitigate the potential
459 off-target effects of piceatannol, we next employed the highly selective SYK inhibitor entospletinib
460 (ENTO; also known as GS-9973) in mock- and FPN-iRPM cultures. Consistently, ENTO
461 effectively suppressed FPN-driven EP enhancement in FPN-iRPMs and iRPMs cultured in ID
462 versus IB serum (Figure 5B-C). Furthermore, we observed that ENTO prevented an increase in
463 Ca^{2+} levels upon FPN overexpression (Figure 5D). Interestingly, supplementation with ENTO was
464 sufficient to reduce both the mitochondrial activity and mass of iRPMs overexpressing FPN to the
465 control levels of mock-transduced cells (Figure 5E-F).

466 Next, we sought to investigate the role of SYK in RPM iron recycling *in vivo.* First, we found that
467 a 4-hour treatment of ID mice with PR73 markedly reduced levels of the active form of SYK,
468 phospho-SYK (Y525/526), in RPMs, whereas no significant effect of the hepcidin agonist was
469 observed in RPMs from IB mice (Figure 5G), similarly to all previous ID-specific suppressive
470 effects of PR73 on RPM rewiring phenotypes. We further assessed the impact of the SYK inhibition
471 with ENTO in both IB and ID mice. Oral daily ENTO administration for the last 2 weeks of the
472 iron-modified diet (5 mg/kg/day; with flavored jellies) effectively reduced phospho-SYK
473 (Y525/526) levels in RPMs from both IB and ID mice compared to vehicle controls (Figure 5H).
474 Strikingly, ENTO administration led to a marked reduction in the EP capacity of RPMs, specifically
475 in ID mice, while EP in IB mice remained unaffected by ENTO treatment (Figure 5I). Furthermore,
476 ENTO treatment partially reversed the increase in Ca^{2+} levels in RPMs observed between ID and
477 IB mice (Figure 5J). Interestingly, ENTO also suppressed FPN induction associated with iron
478 deficiency (Figure 5K), suggesting that EP capacity and FPN expression may be bidirectionally
479 linked. The modulation of FPN appeared independent of liver hepcidin mRNA expression, with no
480 hepcidin induction observed by ENTO supplementation (Figure 5L). Instead, hepcidin expression
481 in ENTO-treated ID mice dropped approximately 50-fold compared to placebo-ID mice. This may
482 indicate that ENTO treatment promotes hepcidin-suppressing signals, such as increased hypoxia
483 or erythropoietic drive, but the exact mechanism by which SYK regulates hepcidin remains to be
484 determined. On systemic levels, a 2-week ENTO treatment did not affect liver iron content within
485 IB or ID groups (Figure S5.2A) or circulating hematological parameters (Figure S5.2B-C), and it

486 only showed some tendency for the more pronounced decrease in the transferrin saturation levels
487 (Figure 5M). Therefore, we extended the period of ENTO administration for 3 weeks and evaluated
488 the systemic blood parameters. While we observed no significant difference in hemoglobin or
489 MCH between iron-restricted mice supplemented with ENTO *versus* placebo (Figure 5N, S5.2D),
490 we noticed an increase in reticulocyte counts and reduction of reticulocyte hemoglobin content
491 (Figure 5O-P), indicating the onset of systemic hematological effects of ENTO treatment.
492 Consistently, whereas erythroid progenitors' expansion was not affected by ID in the bone marrow,
493 we detected a more pronounced expansion of immature EPO-responsive splenic progenitors,
494 proerythroblasts, and EryA erythroblasts, in ENTO-treated *versus* control mice (Figure 5Q-R).
495 Consistently, plasma EPO levels were elevated in a more pronounced manner between ID and IB
496 mice following ENTO supplementation compared to placebo-exposed mice (Figure 5S).
497 Interestingly, the saturation of transferrin in the circulation was not significantly different between
498 ID mice treated with ENTO and placebo (Figure S5.2E). This suggests that a more pronounced
499 compensatory extramedullary erythropoietic response is initiated by ENTO, likely due to less
500 effective direct iron delivery from iron-recycling RPMs. Taken together, SYK activity emerged as
501 critical for the enhanced RBC-clearance capacity of RPMs in ID mice, with SYK inhibition
502 triggering compensatory erythropoietic responses that are consistent with a possible reduction in
503 iron delivery from RPMs.

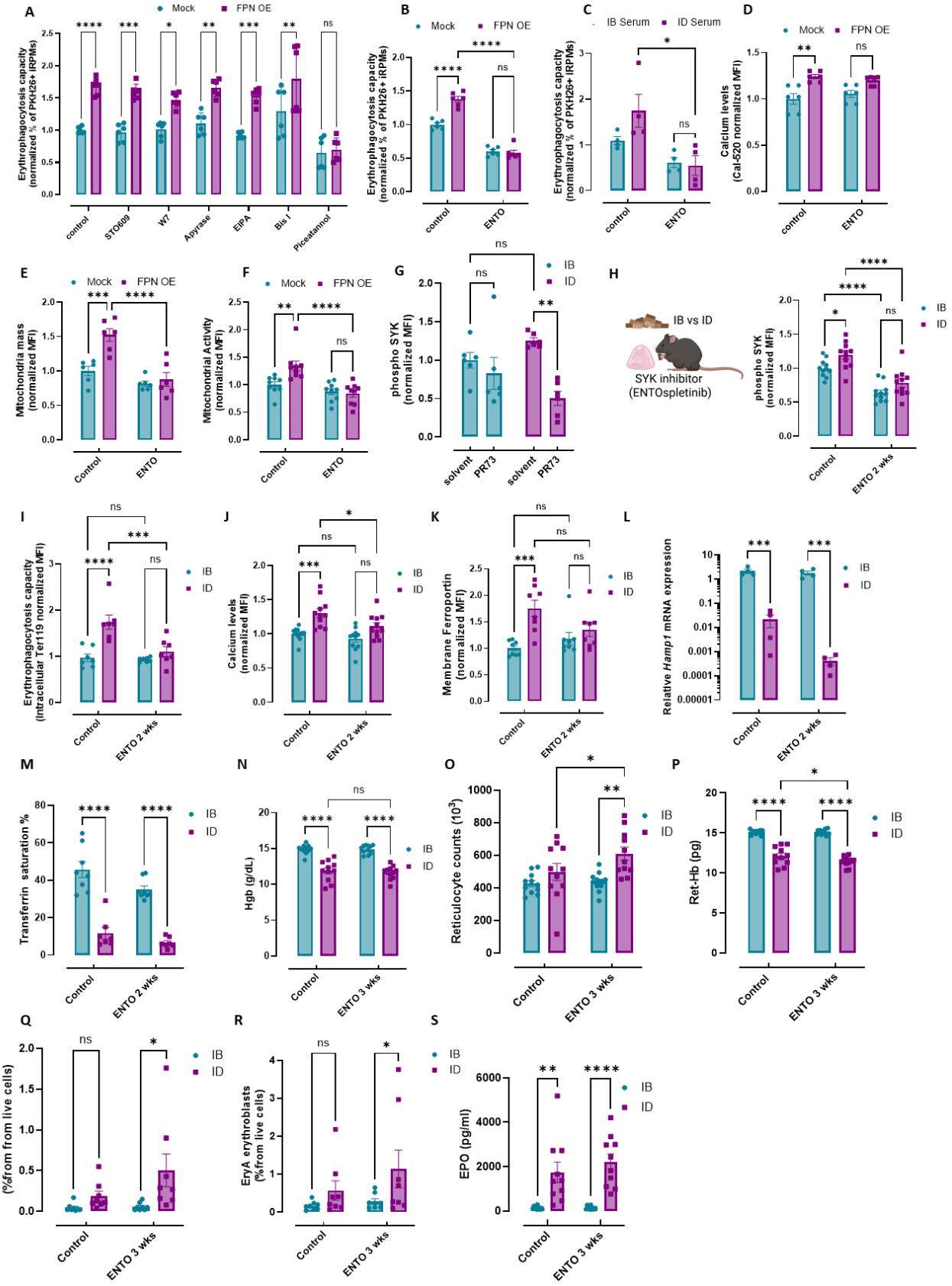
A
Mock
FPN OE
Erythrophagocytosis capacity (normalized % of PKH26+ iRPMs)
control
STO609
W7
Apyrase
EIPA
Bis I
Piceatannol
B
Mock
FPN OE
Erythrophagocytosis capacity (normalized % of PKH26+ iRPMs)
control
ENTO
C
IB Serum
ID Serum
Erythrophagocytosis capacity (normalized % of PKH26+ iRPMs)
control
ENTO
D
Mock
FPN OE
Calcium levels (Cal-520 normalized MFI)
control
ENTO
E
Mock
FPN OE
Mitochondria mass (normalized MFI)
Control
ENTO
F
Mock
FPN OE
Mitochondrial Activity (normalized MFI)
Control
ENTO
G
IB
ID
phospho SYK (normalized MFI)
solvent
PR73
solvent
PR73
H
IB vs ID
SYK inhibitor (ENTOspletinib)
IB
ID
phospho SYK (normalized MFI)
Control
ENTO 2 wks
I
IB
ID
Erythrophagocytosis capacity (Intracellular Ter119 normalized MFI)
Control
ENTO 2 wks
J
IB
ID
Calcium levels (normalized MFI)
Control
ENTO 2 wks
K
IB
ID
Membrane Ferroportin (normalized MFI)
Control
ENTO 2 wks
L
IB
ID
Relative Hamp1 mRNA expression
Control
ENTO 2 wks
M
IB
ID
Transferrin saturation %
Control
ENTO 2 wks
N
IB
ID
Hgb (g/dL)
Control
ENTO 3 wks
O
IB
ID
Reticulocyte counts (10³)
Control
ENTO 3 wks
P
IB
ID
Ret-Hb (pg)
Control
ENTO 3 wks
Q
IB
ID
Proerythroblasts (%from from live cells)
Control
ENTO 3 wks
R
IB
ID
EryA erythroblasts (%from live cells)
Control
ENTO 3 wks
S
IB
ID
EPO (pg/ml)
Control
ENTO 3 wks

504

505 **Figure 5. SYK kinase mediates the FPN-dependent adaptation of RPMs to ID conditions.**

506 (A) Normalized EP capacity of mock and FPN-iRPMs, measured by uptake of PKH26-labeled sRBCs with
507 flow cytometry. iRPMs were cultured with sRBC for 4 days before analysis and treated with inhibitors
508 targeting CaMKK (STO-609; 2.5 μM for 16 hours), ATP-triggered purinergic receptor-mediated Ca^{2+}
509 signaling (Apyrase; 5U/ml for 30 minutes), calmodulin (W7; 20 μM for 30 minutes), macropinocytosis
510 (EIPA; 25 μM for 30 minutes), protein kinase C (Bisindolylmaleimide I, BIS I; 10 μM for 1 hour), and
511 spleen tyrosine kinase (SYK; Piceatannol; 100 μM for 30 minutes). (B) Normalized EP capacity of mock
512 and FPN-iRPMs upon treatment with the SYK inhibitor Entospletinib (ENTO) measured by uptake of
513 PKH26-labeled sRBCs. (C) Normalized EP capacity of iRPMs cultured with serum from IB or ID mice
514 upon treatment with ENTO was measured by uptake of PKH26-labeled sRBCs with flow cytometry. (D)
515 Flow cytometric measurement of cytosolic Ca^{2+} levels in mock and FPN-iRPMs upon treatment with ENTO
516 using Cal-520 fluorescent probe. (E) Mitochondrial mass was determined in mock and FPN-iRPMs upon
517 ENTO treatment using MitoTracker Green and flow cytometry. (F) Mitochondrial activity was measured in
518 mock and FPN-iRPMs with and without treatment with ENTO using the TMRE probe and flow cytometry.
519 (G) Flow cytometric analysis of phosphorylated SYK (phospho-SYK) in RPMs isolated from IB and ID
520 mice, 4 hours after intraperitoneal administration of the hepcidin agonist PR73 (50 nmol/mouse). (H). IB
521 and ID mice were supplemented with the orally bioavailable SYK inhibitor ENTO via daily jelly feeding
522 for two or three weeks before analysis (5 mg/kg/day). Phospho-SYK levels in RPMs were assessed by flow
523 cytometry in IB and ID mice supplemented with ENTO. (I) EP capacity of RPMs from IB and ID mice
524 supplemented with ENTO was determined by intracellular staining for the erythrocyte marker TER119,
525 followed by flow cytometry. (J) Cytosolic Ca^{2+} levels in RPMs from IB and ID mice supplemented with
526 ENTO were measured by flow cytometry using the Cal-520 fluorescent probe. (K) Surface expression of
527 FPN on RPMs was assessed by flow cytometry in IB and ID mice supplemented with ENTO. (L) Relative
528 mRNA expression of the Hamp gene in RPMs from IB and ID mice supplemented with ENTO. (M) Plasma
529 transferrin saturation levels were measured in IB and ID mice supplemented with ENTO. (N) Blood
530 hemoglobin (Hgb) concentration was determined in IB and ID mice supplemented with ENTO. (O)
531 Reticulocyte counts in IB and ID mice supplemented with ENTO. (P) Reticulocyte hemoglobin content in
532 IB and ID mice supplemented with ENTO. (Q and R) Proerythroblast (Q) and EryA erythroblasts (R)
533 representations in the spleens of IB and ID mice supplemented with ENTO. (S) Plasma EPO levels were
534 measured in IB and ID mice supplemented with ENTO. Each dot represents either an independent cell-
535 based experiment or one mouse. Data are represented as mean ± SEM. Two-way ANOVA with Tukey's
536 Multiple Comparison tests was used to determine statistical significance. ns $p>0.05$, *$p<0.05$, **$p<0.01$,
537 ***$p<0.001$ and ****$p<0.0001$.

538 **Functional adaptation of RPMs to iron deficiency involves enhanced BCAA catabolism and**
539 **β-oxidation pathways**

540 Efferocytosis is a continuous, energy-intensive process that demands extensive metabolic resources
541 and reprogramming[59]. Enhanced glucose uptake and potentiated OXPHOS of ID *versus* IB RPMs,
542 processes regulated in part by FPN (Figure 3N and P), have been previously reported to support
543 efferocytosis[9,10]. However, we questioned whether the metabolic reprogramming observed in
544 RPMs of ID mice reflects a unique adaptation to the challenge of processing hemoglobin-rich
545 RBCs or if it shares features with other macrophage efferocytic programs. To address this, we
546 revisited our transcriptomic and proteomic datasets. Morioka *et al*. identified nineteen solute carrier
547 (SLC) transporter genes that are transcriptionally upregulated during apoptotic cell clearance,

548 establishing a canonical efferocytosis signature[9]. Strikingly, RPMs in ID mice diverge from this
549 model: none of these nineteen SLC transporters were upregulated at the mRNA level. Notably,
550 RPMs also failed to display detectable protein levels of key enzymes associated with amino acid
551 signaling that support efferocytosis, including ARG1 and ODC1 (crucial for arginine-to-putrescine
552 conversion), or IDO1 (the tryptophan-catabolizing enzyme), and did not express SLC36A4, the
553 principal tryptophan transporter[15,17]. While GLS1, the enzyme responsible for non-canonical
554 glutaminolysis[18], was detected through proteomic analysis, its levels were unaltered under iron-
555 deficient conditions. Conversely, the enriched category of metabolic proteins differentially
556 regulated in RPMs of ID mice revealed consistent alterations of lipid metabolism, resembling other
557 efferocytic macrophages[10]. This includes elevated enrichment expression of β-oxidation enzymes,
558 most notably the rate-limiting CPT2, induction of lipases, and concurrent downregulation of
559 DGAT1 (diacylglycerol O-acyltransferase 1), which mediates triacylglyceride synthesis.
560 Interestingly, we also observed significant enrichment of enzymes involved in branched-chain
561 amino acid (BCAA) breakdown. In parallel, two upregulated proteomic hits, SLC7A7 and
562 SLC7A8, represent antiporters that transport cationic and large neutral amino acids, including
563 BCAAs[60].

564 To validate these metabolic adaptations in RPMs of ID mice and assess whether they are specific
565 to this subset, we profiled selected proteomic hits by flow cytometry across tissue-resident
566 macrophage populations. We found that BCKDHB, the rate-limiting enzyme of BCAA catabolism,
567 the BCAA exporter SLC7A7, β-oxidation enzymes CPT2 and ACADSB, the TCA enzyme citrate
568 synthase, and the lipase ABHD12B were all significantly elevated in ID RPMs compared to iron-
569 balanced controls, while remaining unchanged or reduced in KCs and peritoneal macrophages
570 (Figure 6A). Consistently, both DGAT1 and lipid droplet levels were specifically downregulated
571 in RPMs of ID mice, suggesting a unique skewing toward energy-consuming pathways under iron
572 deficiency (Figure 6A). Next, we focused on BCAA metabolism, a pathway not previously linked
573 to enhanced efferocytosis. Baseline BCAA levels were exceptionally high in RPMs compared to
574 other splenic cell types, though still lower than in KCs and similar to peritoneal macrophages
575 (Figure 6B-C). BCAA content increased significantly in RPMs treated *ex vivo* with ERG240, a
576 pharmacologic blocker of BCAA catabolism at the stage of the first reaction catalyzed by the BCAT
577 enzyme (Figure 6C). Prolonged exposure of iRPMs to stressed RBCs, but not RBC ghosts, induced
578 strong BCKDHB expression, more robust than in standard BMDMs, and appeared to prevent

579 BCAA accumulation in RBC-exposed cells (Figure 6D-E). Notably, BCAA content remained
580 unchanged in RPMs from ID mice (Figure 6F), despite elevated EP, suggesting that BCAA
581 metabolism is tightly regulated. This implied that ID conditions impose a new metabolic
582 equilibrium necessary to maintain enhanced iron recycling by RPMs. Further exploring this
583 concept, BCKDHB levels were elevated in iRPMs overexpressing FPN, a response that, like EP,
584 depended on both FPN and SYK kinase activity (Figure 6G). The SYK dependency of BCKDHB
585 was also evident *in vivo* in RPMs derived from ID *versus* IB mice (Figure 6H). Strikingly, inhibition
586 of BCAT enzymatic activity using ERG240 abolished the EP boost caused by FPN overexpression
587 (Figure 6I), indicating that enhanced BCAA catabolism is essential for reprogramming RPM
588 phagocytic function. Similarly, exposure to leucine increased EP capacity in iRPMs in a manner
589 diminished by ERG240 pre-treatment (Figure 6J). Interestingly, BCAT inhibition also reversed
590 BCKDH induction and reduced mitochondrial mass and activity, specifically in FPN-
591 overexpressing iRPMs (Figure 6K-M). We confirmed the reversal of the enhanced phagocytic and
592 metabolic function of ID-like RPMs by BCAT suppression using another inhibitor, BAY069
593 (Figure S6.1A-C). We next looked at the requirement of β-oxidation for the RPM ID-like
594 adaptation. Like BCKDHB, CPT2 upregulation was dependent on both FPN and SYK activity
595 (Figure S6.2A). This SYK dependence was further validated *in vivo*, where ENTO reversed CPT2
596 induction in RPMs from ID mice (Figure S6.2B). Finally, inhibition of CPT2 activity with
597 trimetazidine (TMZ) abolished the enhanced EP observed with FPN overexpression, demonstrating
598 that increased β-oxidation is a key component of the metabolic programming driving augmented
599 phagocytic function in RPMs (Figure S6.2C). Taken together, both BCAA catabolism and β-
600 oxidation emerged in our study as FPN/SYK-controlled pathways that maintain enhanced
601 phagocytosis and metabolic activities of RPMs in iron deficiency.

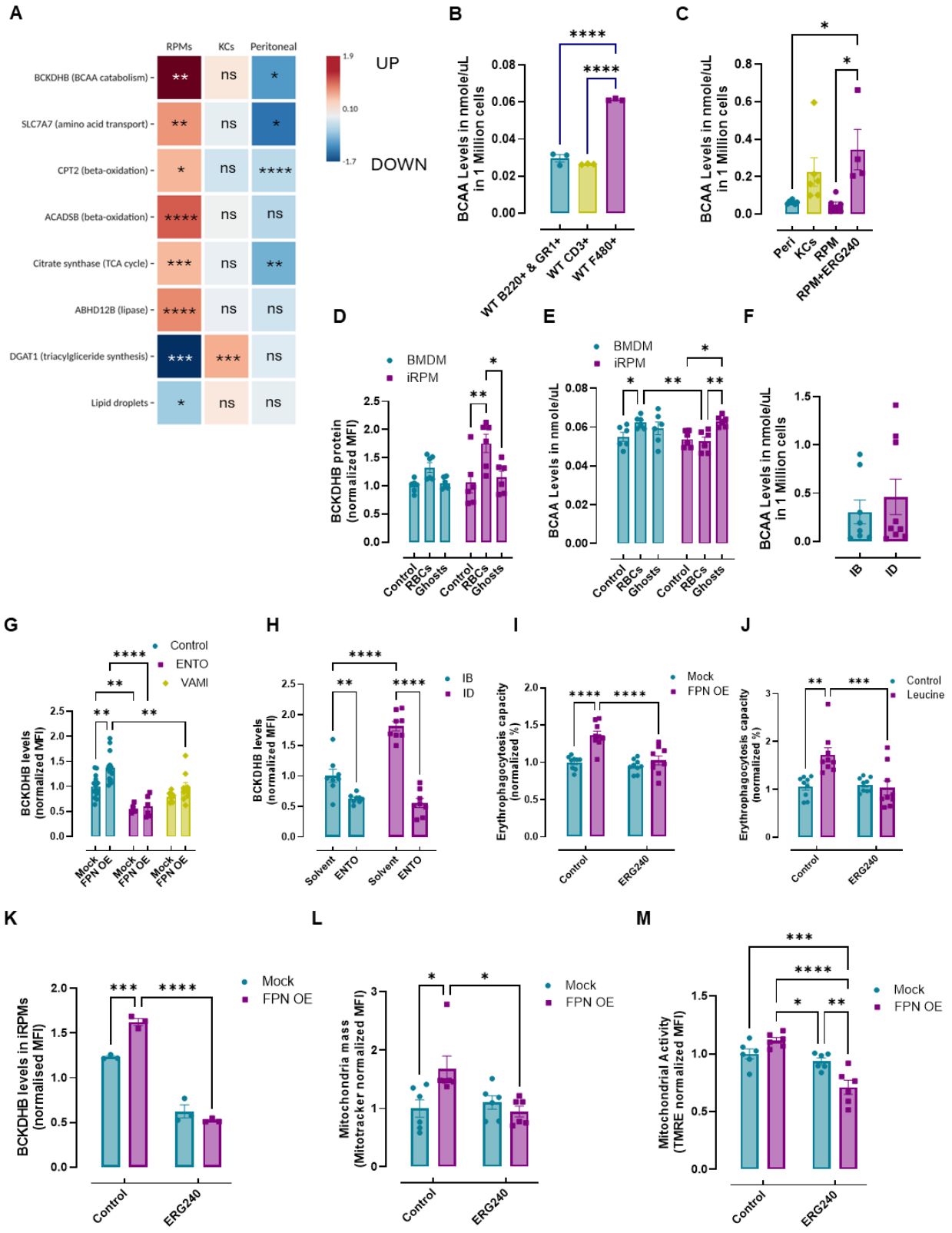
A
RPMs
KCs
Peritoneal
BCKDHB (BCAA catabolism)
SLC7A7 (amino acid transport)
CPT2 (beta-oxidation)
ACADSB (beta-oxidation)
Citrate synthase (TCA cycle)
ABHD12B (lipase)
DGAT1 (triacylgliceride synthesis)
Lipid droplets
UP
DOWN
B
BCAA Levels in nmole/uL in 1 Million cells
WT B220+ & GR1+
WT CD3+
WT F480+
C
Peri
KCs
RPM
RPM+ERG240
D
BMDM
iRPM
BCKDHB protein (normalized MFI)
Control
RBCs
Ghosts
E
BCAA Levels in nmole/uL
F
IB
ID
G
Control
ENTO
VAMI
BCKDHB levels (normalized MFI)
Mock
FPN OE
H
Solvent
I
Erythrophagocytosis capacity (normalized %)
ERG240
J
Leucine
K
BCKDHB levels in iRPMs (normalised MFI)
L
Mitochondria mass (Mitotracker normalized MFI)
M
Mitochondrial Activity (TMRE normalized MFI)

605 **Figure 6. Functional adaptation of RPMs to iron deficiency involves enhanced BCAA catabolism.**

606 (A) Heatmap showing levels of BCKDHB, SLC7A7, CPT2, ACADSB, citrate synthase, ABHD12B,
607 DGAT1, and lipid droplet levels across RPMs, KCs, and peritoneal macrophages measured by flow
608 cytometry. Data represent log2-transformed fold changes in cells of ID mice vs IB mice, with significant
609 changes marked by asterisks. (B) Quantification of BCAA levels in different splenic immune cell
610 populations - F4/80$^+$ RPMs, CD3$^+$ T cells, and other splenocytes, measured using a colorimetric BCAA
611 assay. (C) Quantification of BCAA levels of *ex vivo* magnetically-sorted peritoneal macrophages, KCs, and
612 RPMs (untreated and treated with ERG240). (D) Intracellular BCKDHB levels and (E) BCAA levels in
613 iRPMs and BMDMs treated with stressed RBCs and RBC ghosts compared to untreated control. (F) BCAA
614 levels in magnetically-isolated RPMs from IB and ID mice (G). Intracellular BCKDHB levels in mock and
615 FPN overexpressing (OE) iRPMs upon treatment with entospletinib (ENTO) (10 μM, 1 h) and vamifeport
616 (VAMI) (20 μM, 15 h), determined using flow cytometry (H). Intracellular BCKDHB levels in RPMs from
617 IB and ID mice supplemented with ENTO via jelly feeding (3 weeks) were determined using flow
618 cytometry. (I) Normalized EP capacity towards PKH26-sRBCs by mock and FPN overexpressing iRPMs
619 upon ERG240 treatment (10 μM, 15 h). (J) Normalized EP capacity towards PKH26-sRBCs by iRPMs upon
620 leucine exposure. (K) Intracellular BCKDHB levels in mock and FPN OE iRPMs upon treatment with
621 ERG240. (L) Mitochondrial mass was determined in mock and FPN OE iRPMs upon treatment with
622 ERG240 using MitoTracker Green and flow cytometry. (M) Mitochondrial activity was determined in mock
623 and FPN OE iRPMs upon treatment with ERG240 using the TMRE probe and flow cytometry. Each dot
624 represents one mouse or an independent cell-based experiment. Data are represented as mean ± SEM. Two-
625 way ANOVA with Tukey's Multiple Comparison tests was used in D, E, and G-M, while one-way ANOVA
626 test with Dunnett's or Tukey's Multiple Comparison tests was used in B and C, A Welch's unpaired t-test
627 determined statistical significance in A and F. ns $p>0.05$, *$p<0.05$, **$p<0.01$, ***$p<0.001$ and
628 ****$p<0.0001$.

629 ***In vivo* inhibition of BCAA catabolism alters erythrophagocytic capacity and metabolic**
630 **remodeling of RPMs in ID mice**

631 We next sought to dissect the functional relevance of BCAA metabolism in regulating
632 erythrophagocytic capacity and mitochondrial remodeling *in vivo*. First, we found that enhanced
633 OXPHOS of freshly isolated RPMs from ID mice, as measured using a Seahorse analyzer, was
634 abrogated by *ex vivo* treatment with ERG240 (Figure 7A), indicating its critical dependence on
635 BCAA catabolism. Next, we administered ERG240, a bioavailable BCAT inhibitor, to ID mice via
636 daily jelly feeding for three weeks. Consistent with our *in vitro* observations, ERG240 treatment
637 significantly suppressed the enhanced EP activity of RPMs in ID mice (Figure 7B). In parallel,
638 ERG240 administration prevented the increase of mitochondrial mass and the upregulation of
639 BCKDHB and citrate synthase protein levels, a proxy for TCA cycle capacity (Figure 7C-E).
640 Interestingly, despite this reduction in mitochondrial mass and citrate synthase, mitochondrial
641 membrane potential was not suppressed and remained comparable to untreated ID controls (Figure
642 7F), suggesting a partial uncoupling between mitochondrial polarization state and respiratory
643 functions under conditions of BCAT inhibition *in vivo*. Notably, FPN protein abundance remained

644 unchanged in ERG240-treated mice subjected to ID feeding (Figure 7G), indicating that, as in
645 ENTO-supplemented animals, reduced RPM erythrophagocytic activity is linked to diminished
646 exposure of FPN at the plasma membrane. At the systemic level, ERG240 treatment very modestly
647 affected the degree of anemia, as evidenced by a slightly more pronounced reduction in hematocrit,
648 while hemoglobin levels, MCV, and MCH values remained unchanged in ID mice receiving the
649 drug relative to untreated ID controls (Figure 7H and S7A). However, circulating reticulocyte
650 counts were significantly elevated specifically in ERG240-treated animals (Figure 7I), indicating
651 a heightened stress erythropoietic response aimed at restoring circulating red cell mass, likely
652 reflecting enhanced sensing of iron deficiency. In line with this, ERG240-treated mice displayed a
653 significant expansion of splenic erythroid progenitors, with both proerythroblasts and EryB
654 erythroblasts (Figure S7D) showing elevated representation relative to untreated ID mice.
655 Consistently, plasma EPO levels were significantly elevated in ERG240-treated ID mice (Figure
656 7J), aligning with the observed expansion of splenic erythroid progenitors. Interestingly, not only
657 were *Epo* mRNA levels elevated in the kidney of ID mice upon ERG240 supplementation as
658 compared to placebo controls, but also *Tfrc* transcription was increased (Fig. 7K and L). Similarly,
659 cardiac *Tfrc* appeared as more significantly induced in ID mice upon ERG240 treatment compared
660 with untreated ID controls, reflecting a slightly more pronounced drop in the heart non-heme iron
661 content (Fig. S7E-F). However, liver *Tfrc* induction and a decrease in iron levels upon ID diet were
662 not modified by ERG240 supplementation (Fig. S7G-H), and transferrin saturation remained
663 comparably reduced in ERG240- and placebo groups (Fig. S7I). These observations may suggest
664 sensing of more pronounced hypoxia by the kidney, and of tissue iron deficiency in some, but not
665 organs.

666 Finally, to assess how systemic iron deficiency alters mitochondrial fuel use *in vivo*, and how these
667 changes depend on BCAT activity, we performed MitoPlate S1 substrate profiling on freshly
668 isolated RPMs. Relative to IB controls, RPMs from ID mice exhibited broadly increased utilization
669 of glycolytic, amino-acid–derived, fatty-acid/carnitine-linked, and TCA cycle substrates,
670 consistent with their heightened OXPHOS phenotype (Figure 7M). BCAT inhibition with ERG240
671 partially attenuated this shift, most notably reducing oxidation of several TCA cycle and fatty-acid–
672 linked fuels, in line with the decrease in global mitochondrial respiration measured by Seahorse.
673 In contrast, several amino-acid substrates, such as leucine+L-malic acid, tryptamine, and ornithine,
674 remained more highly utilized than in IB RPMs, indicating that while BCAT-dependent BCAA

675 metabolism contributes to the enhanced respiratory capacity of ID RPMs, additional metabolic
676 pathways support the full extent of their increased mitochondrial activity.

677 Collectively, these data demonstrate that BCAA catabolism is required for sustaining increased EP
678 functions, with implications for the body's adaptation to dietary iron restriction.

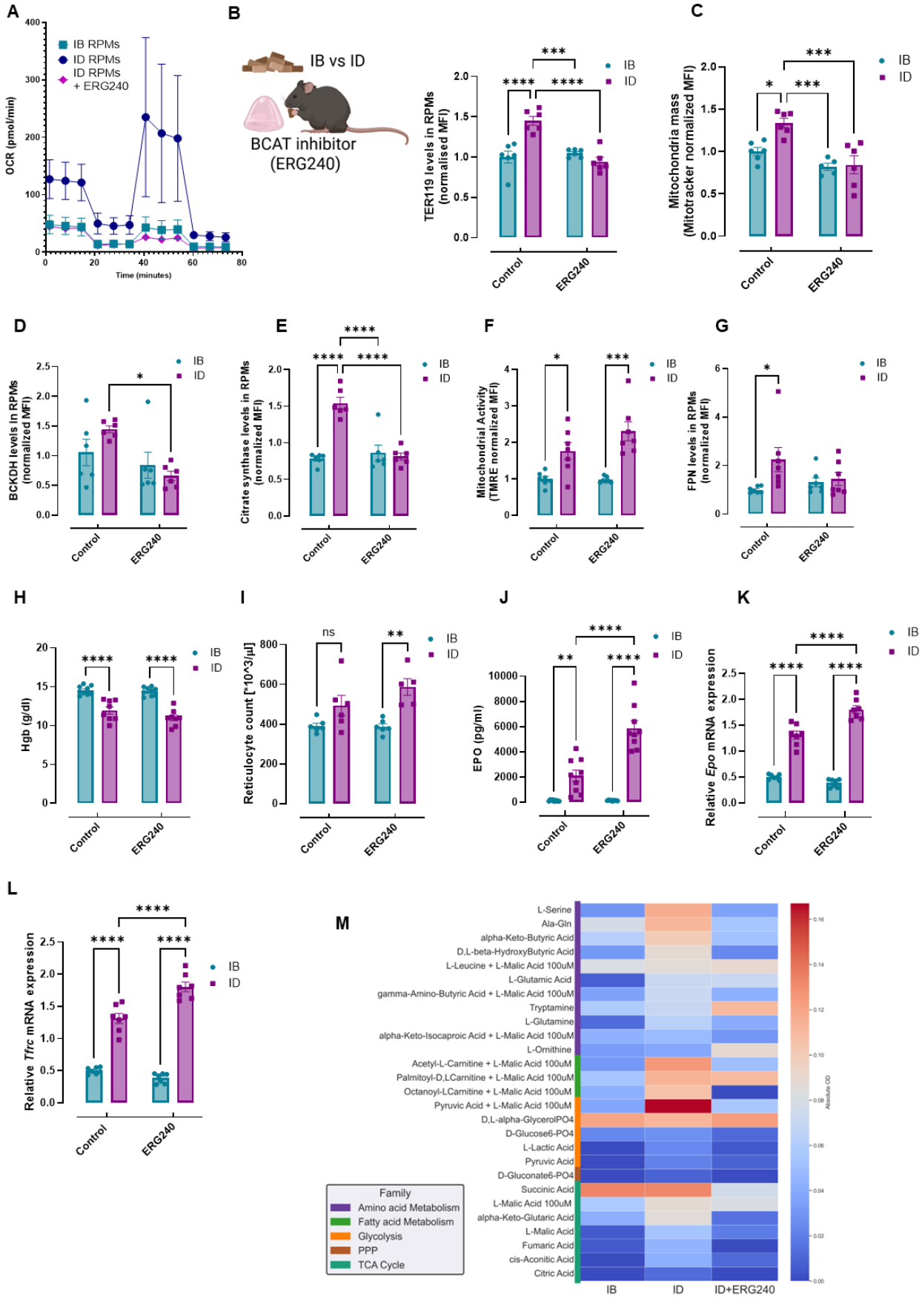
A
IB RPMs
ID RPMs
ID RPMs + ERG240
OCR (pmol/min)
Time (minutes)
B
IB vs ID
BCAT inhibitor (ERG240)
TER119 levels in RPMs (normalised MFI)
Control
ERG240
C
Mitochondria mass (Mitotracker normalized MFI)
D
BCKDH levels in RPMs (normalized MFI)
E
Citrate synthase levels in RPMs (normalized MFI)
F
Mitochondrial Activity (TMRE normalized MFI)
G
FPN levels in RPMs (normalized MFI)
H
Hgb (g/dl)
I
Reticulocyte count [*10^3/µl]
J
EPO (pg/ml)
K
Relative Epo mRNA expression
L
Relative Tfrc mRNA expression
M
L-Serine
Ala-Gln
alpha-Keto-Butyric Acid
D,L-beta-HydroxyButyric Acid
L-Leucine + L-Malic Acid 100uM
L-Glutamic Acid
gamma-Amino-Butyric Acid + L-Malic Acid 100uM
Tryptamine
L-Glutamine
alpha-Keto-Isocaproic Acid + L-Malic Acid 100uM
L-Ornithine
Acetyl-L-Carnitine + L-Malic Acid 100uM
Palmitoyl-D,LCarnitine + L-Malic Acid 100uM
Octanoyl-LCarnitine + L-Malic Acid 100uM
Pyruvic Acid + L-Malic Acid 100uM
D,L-alpha-GlycerolPO4
D-Glucose6-PO4
L-Lactic Acid
Pyruvic Acid
D-Gluconate6-PO4
Succinic Acid
L-Malic Acid 100uM
alpha-Keto-Glutaric Acid
L-Malic Acid
Fumaric Acid
cis-Aconitic Acid
Citric Acid
IB
ID
ID+ERG240
Absolute OD
Family
Amino acid Metabolism
Fatty acid Metabolism
Glycolysis
PPP
TCA Cycle

679

680 **Figure 7. *In vivo* inhibition of BCAA catabolism alters erythrophagocytic capacity and metabolic**
681 **remodeling of RPMs in ID mice.**

682 (A) Seahorse analysis of *ex vivo* magnetically-isolated RPMs from IB and ID mice, including 4-hour ERG240
683 preincubation for RPMs from ID mice. (B) IB and ID mice were supplemented with the orally bioavailable BCAT
684 inhibitor ERG240 via daily jelly feeding for three weeks before analysis (5 mg/kg/day). EP capacity of RPMs
685 from IB and ID mice supplemented with ERG240, determined by intracellular staining for the erythrocyte marker
686 TER119, followed by flow cytometry. (C) Mitochondrial mass of RPMs from IB and ID mice supplemented with
687 ERG240 was determined using MitoTracker Green, followed by flow cytometry. (D) Intracellular BCKDHB
688 levels of RPMs from IB and ID mice supplemented with ERG240 (E). Intracellular citrate synthase levels of
689 RPMs from IB and ID mice supplemented with ERG240 (F). Mitochondrial activity of RPMs from IB and ID
690 mice supplemented with ERG240 was determined using the TMRE probe, followed by flow cytometry. (G) FPN
691 levels of RPMs from IB and ID mice supplemented with ERG240 were determined by flow cytometry. (H) Blood
692 hemoglobin (Hgb) and reticulocyte count (I) were determined in IB and ID mice supplemented with ERG240.
693 (J) Plasma EPO levels were measured in IB and ID mice supplemented with ERG240. (K and L) Relative mRNA
694 expression of the (K). Relative mRNA expression of *Epo* and (L) *Tfrc* genes in the kidneys of IB and ID mice
695 supplemented with ERG240 (M). Absolute mitochondrial substrate utilization profiles of RPMs from IB, ID, and
696 ID mice supplemented with ERG240, measured using the MitoPlate S1 assay. Blank-corrected OD values for all
697 metabolites with detectable activity in ID RPMs (n = 27) are shown and grouped by metabolic pathway. Each
698 dot represents one mouse or an independent cell-based experiment. Data are represented as mean ± SEM. Two-
699 way ANOVA with Tukey's Multiple Comparison tests was used in B-L. ns $p>0.05$, *$p<0.05$, **$p<0.01$,
700 ***$p<0.001$ and ****$p<0.0001$.

701

702 **DISCUSSION**

703 Iron deficiency is a complex physiological state with multifaceted implications. The precise
704 quantitative thresholds that trigger cellular or organismal functional consequences, and the cell-
705 type-specific molecular consequences, including the identification of the most vulnerable cell types
706 and the sequence of cellular dysfunction triggered by iron deficiency, remain poorly understood.
707 Beyond its well-known erythropoietic effects that lead to anemia, iron deficits also impact neuronal
708 and myocyte function[29,61,62], and alter immune cell activity, with studies demonstrating impaired
709 lymphocyte proliferation[63,64] and dysregulated macrophage responses[28,29]. However, much of our
710 understanding of macrophage iron metabolism comes from *in vitro* studies or models that may not
711 fully capture the complexity of *in vivo* iron deficiency. The seemingly contradictory findings
712 regarding the effects of iron depletion on macrophage inflammatory cytokine production *in vitro*
713 versus *in vivo*[47,65,66] highlight the critical need for a more incisive, cell-type-specific, and context-
714 dependent understanding of iron's role in macrophage function. Specifically, how RPMs,
715 specialized iron-recycling cells central to the maintenance of systemic iron homeostasis, adapt to
716 the metabolic stress of systemic iron deficiency remains a key open question. Here, we address this

717 gap by defining a signaling-metabolic circuit through which systemic iron deficiency reprograms
718 RPMs to enhance erythrophagocytosis and sustain iron recycling (Fig. 8).

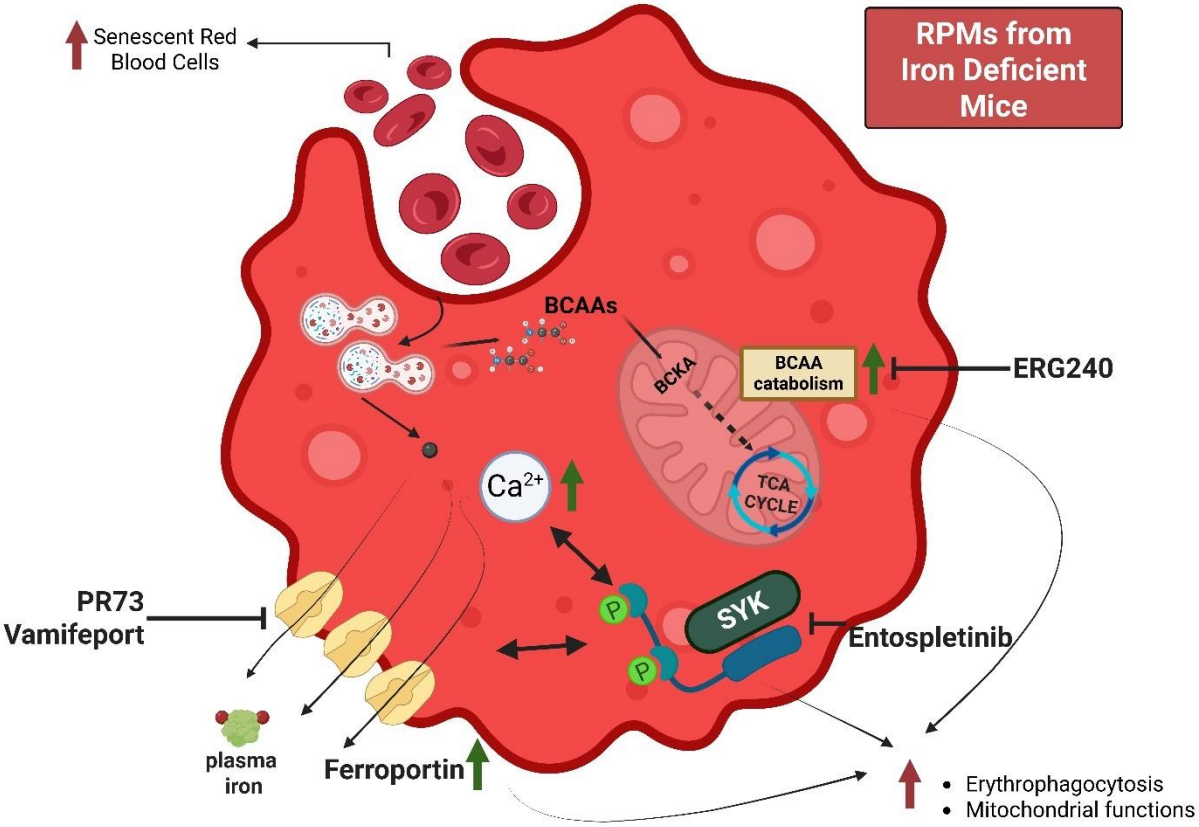

719
720 **Figure 8. Iron deficiency induces metabolic rewiring of red pulp macrophages to enhance**
721 **erythrophagocytosis.**

722 Model illustrating how systemic iron deficiency reprograms RPMs to sustain iron recycling. Increased FPN-
723 mediated iron export activates SYK-dependent signaling, promoting mitochondrial metabolic adaptation,
724 including BCAA catabolism, which supports enhanced erythrophagocytosis of senescent RBCs.
725 Pharmacological inhibition of FPN, SYK, or BCAA catabolism disrupts this adaptive program.

726 RPMs from ID mice displayed classical markers of cellular iron depletion (increased TFR1,
727 decreased ferritin), reflecting activation of the iron-responsive element/iron regulatory protein
728 (IRE/IRP) system, a post-transcriptional regulatory mechanism that normally increases iron uptake
729 and reduces iron storage and FPN-mediated export under iron-limiting conditions[19,67]. However,
730 we observed increased FPN expression in RPMs of ID mice, despite proteomic analysis showing
731 elevated IRP2 levels. This implies that suppressed hepcidin levels in iron deficiency, which relieve
732 the dominant negative regulation of FPN, override any potential IRP2-mediated repression.
733 Although RPM iron stores were low in ID mice, increased LIP and oxidative stress were observed
734 relative to IB controls, consistent with enhanced EP activity and a likely increase in cellular iron

735 flux. Intriguingly, this observation suggests that other iron-related signals beyond LIP contribute
736 to IRP2 stabilization in RPMs. The elevated FPN expression facilitates the export of iron derived
737 from engulfed RBCs, likely supporting the accelerated stress erythropoiesis in the spleen and the
738 iron needs of other cell types during iron deficiency. These results reveal an adaptive mechanism
739 in RPMs, prioritizing systemic iron delivery over maintenance of circulating RBCs or cellular iron
740 retention in RPMs during deficiency.

741 The established cellular response to iron deficiency, frequently modeled through TFR1 disruption,
742 involves a metabolic shift towards glycolysis, accompanied by mitochondrial dysfunction, and
743 impairments in the electron transport chain[68]. In contrast, RPMs from ID mice show enhanced
744 mitochondrial function, with increased mitochondrial mass and elevated OXPHOS activity
745 confirmed by Seahorse and proteomic analyses, accompanied by an increase in mitochondrial
746 membrane potential. This unique, cell-type-specific metabolic adaptation, absent in Kupffer cells
747 and peritoneal macrophages, suggests that RPMs are exceptional in adjusting their physiology to
748 increased bioenergetic demand, imposed by boosted iron recycling capability. Whether these
749 responses are driven by the spleen's unique microenvironment, potentially via signals from
750 extramedullary erythropoiesis, remains to be understood. Importantly, this exceptional metabolic
751 state of highly enhanced mitochondrial respiration was acutely shut down by inhibition of FPN
752 with PR73, and mirrored by suppressed glucose uptake and protein synthesis *in vivo*, pointing to a
753 novel relationship between FPN functionality and cellular metabolism in the context of heightened
754 efferocytic activity. These findings were further supported by the similar metabolic features
755 induced solely by FPN overexpression in the RPM *in vitro* model.

756 Emerging evidence links substantial metabolic reprogramming to efferocytosis. This is hallmarked
757 by altered amino acid utilization, particularly of arginine[15], methionine[16], tryptophan[17], and
758 glutamine[18], lactate production[8,9], boosted pentose phosphate pathway[13,14], increased glucose
759 uptake and glycolysis[8,9], fatty acid oxidation[10], and, critically, enhanced mitochondrial
760 respiration[11,12], acting in concert to sustain energetically demanding efferocytosis and promote an
761 anti-inflammatory milieu[11,12]. While RPMs of ID mice retain some of these metabolic traits,
762 particularly enhanced OXPHOS, our omics analyses reveal a distinct divergence from canonical
763 efferocytic programs. For example, key transporters and enzymes involved in arginine, tryptophan,
764 and glutamine metabolism are absent or uninduced. BCAAs represent important metabolic
765 substrates for macrophages, fueling the TCA cycle and supporting both pro-inflammatory and anti-

766 inflammatory polarization in a context-dependent manner [69–71]. However, the relevance of BCAA
767 catabolism in promoting efferocytosis and controlling the functions of iron-recycling macrophages
768 has remained largely unexplored. Our study demonstrates that RPMs of ID mice uniquely
769 upregulate BCKDHB in a manner controlled by both FPN and SYK, identifying the new
770 mechanistic link between the capacity of BCAA breakdown and these regulators. We further show
771 that enhanced RBC clearance in RPMs relies on BCAA-driven bioenergetics, reflected by the
772 dependence of their heightened OXPHOS on BCAT activity. Our MitoPlate profiling further
773 clarifies this metabolic specialization. Although RPMs from ID mice display broadly elevated
774 mitochondrial substrate use, BCAT inhibition led to a marked divergence between fuel classes:
775 oxidation of several key TCA cycle and fatty-acid–linked substrates was substantially reduced by
776 ERG240, whereas utilization of select amino-acid–derived fuels, particularly leucine, malic acid,
777 tryptamine, and ornithine, remained comparatively resilient. This pattern points to a reliance on
778 non-canonical transamination-linked anaplerosis that sustains the α-ketoglutarate (α-KG) pool.
779 When BCAT is suppressed, the diminished α-KG supply limits TCA cycle flux, making
780 conventional carbon inputs more vulnerable, while specific amino acid pathways able to restore or
781 utilize α-KG through distinct enzymatic routes can still support the elevated mitochondrial state
782 characteristic of RPMs in ID mice. Altogether, these findings reveal either a previously
783 unrecognized specialization of RPMs for processing BCAA-rich RBCs or suggest a more general,
784 therapeutically exploitable metabolic dependency in efferocytic macrophages. Future work will
785 clarify whether this pathway is restricted to RPMs or is required for efficient or increased clearance
786 of apoptotic cells in other macrophage subtypes.

787 Our work further identified significantly elevated intracellular Ca^{2+} levels in RPMs of ID mice,
788 closely dependent on functional FPN and correlating with their enhanced EP capacity. While recent
789 studies have demonstrated that PKC activity can promote FPN exposure on the cell surface in type
790 2 diabetes and as a response to iron loading[72], our findings suggest that, in the context of iron
791 deficiency, increased FPN expression and elevated intracellular Ca^{2+} may represent parallel or
792 intersecting pathways that together facilitate enhanced EP. It is also plausible that RPMs of ID
793 mice, characterized by low iron stores but elevated LIP, additionally regulate FPN exposure on the
794 surface via Ca^{2+}-stimulated high PKC activity. Our data suggest no direct involvement of PKC in
795 mediating FPN-dependent and Ca^{2+}-triggered regulation of EP, at least using the cellular model of
796 RPMs. However, RPMs of ID mice treated by ENTO not only downmodulate EP but also FPN

797 surface levels and Ca^{2+}, which may represent a secondary response, possibly mediated by PKC
798 activity.

799 Our discovery that SYK drives EP in RPMs aligns with its emerging roles in diverse phagocytic
800 processes. Bian *et al*. demonstrated that SYK activation overrides Cd47-SIRPα-mediated "don't
801 eat me" signals to enable inflammation-driven clearance of "self" RBC[26]. Recent studies highlight
802 SYK as a critical mediator of microglial responses to amyloid-β (Aβ) plaques in Alzheimer's
803 disease, where SYK deficiency impairs Aβ phagocytosis[73,74]. Our work extends this observation
804 by identifying iron deficiency as a physiological trigger for SYK activation in RPMs, with
805 upstream regulation by the low hepcidin-high FPN. Furthermore, our work reveals SYK-dependent
806 metabolic-phagocytic coupling. Whereas previous findings link high SYK activity to inhibition of
807 mitochondrial respiration[75], we show that mitochondrial membrane potential and mass, heightened
808 by FPN overexpression, critically depend on SYK activity. Critically, our data imply that SYK may
809 represent a novel molecular switch for the regulation of efferocytic capacity, a concept that requires
810 further work.

811 Finally, the FPN–SYK-mediated rewiring of RPMs in iron deficiency does not resemble M1/M2-
812 like polarization. RPMs from ID mice exhibited an ambiguous pattern of surface marker
813 alterations, indicating no consistent pro- or anti-inflammatory skewing, and no clear regulation of
814 immune-linked mediators in omics data. They also employed a mixed functional phenotype:
815 elevated ROS production, driven by increased labile iron, characteristic of M1 macrophages,
816 alongside enhanced oxidative phosphorylation, mitochondrial biogenesis, and lysosomal activity,
817 features typically associated with M2 macrophages[76–82]. Together with the notion that enhanced EP
818 in RPMs only partially resembles previously reported adaptation mechanisms to efferocytosis, our
819 work proposes that the polarization state of RPMs in iron deficiency represents a new type of
820 adaptation, whose resemblance in other macrophage types/environmental conditions opens an
821 avenue for future investigations. Likewise, our findings highlight the need to determine how RPM
822 adaptations and increased EP during iron deficiency reshape iron redistribution among tissues, and
823 how these metabolic shifts may ultimately influence organismal functions such as immune
824 responses, neuronal activity, and muscle performance.

825 **Methods**

826 **Mice**

827 Female C57BL/6 J mice were utilized for the experiments and housed under specific pathogen-free
828 (SPF) conditions at the Experimental Medicine Centre in Bialystok, Poland. These mice were
829 provided with either a standard iron-balanced diet (200 mg/kg, SAFE U8958P; IB diet) or an iron-
830 deficient diet (5.9 mg/kg, SAFE U8958P; ID diet) for 5 weeks, commencing at 4 weeks of age. 9-
831 week-old *Tmprss6* wild-type and KO mice were provided by Dr. Delphine Meynard from
832 INSERM, Toulouse, France. Upon arrival at the local facility at the International Institute of
833 Molecular and Cell Biology (IIMCB), mice were acclimatized briefly before being sacrificed or
834 subjected to further procedures, if required. Ms4a3-Cre mice were obtained from Florent
835 Ginhoux[40], and RosaTdT reporter mice [B6;129S6-Gt(ROSA)26Sortm9(CAG-tdTomato)Hze/J
836 JAX#: 007905] were a kind gift of Agnieszka Kobielak. Female C57BL/6-Tg(UBC-GFP)30Scha/J
837 (UBI-GFP/BL6) mice were kindly provided by Aneta Suwińska (Faculty of Biology, University of
838 Warsaw, Poland). For primary cell cultures, C57BL/6 J mice were maintained in the SPF facility
839 at the Mossakowski Medical Research Institute in Warsaw, Poland. All animal experiments and
840 protocols were approved by the respective local ethical committees in Olsztyn and Warsaw,
841 including the decisions: Uchwala 026, WAW2/015/2019, and WAW2/048/2020). Usage of
842 Ms4a3Cre-RosaTdT reporter mice was approved by WAW2/126/2023. For PR73 administration,
843 mice were intraperitoneally injected with 50 nmol of PR73 for 4 hours before being sacrificed. The
844 procedure was approved by the local ethical committee in Warsaw (WAW2/150/2019).
845 Experiments including SYK and BCAA catabolism suppression were covered by the permissions:
846 WAW2/068/2024 and WAW2/029/2025.

847

848 **Isolation of Single-Cell Suspensions from Murine Organs**

849 Bone marrow cells were obtained by flushing the femurs and tibias with sterile HBSS (Gibco,
850 14025092) using a 25G needle. Following centrifugation at 600 x g for 10 minutes at 4°C, the pellet
851 containing the isolated cells was collected for further processing. The spleen was harvested and
852 homogenized by passage through a 70 µm cell strainer (pluriSelect, 43-50070-51). Before FACS
853 sorting, the spleen was enzymatically digested with HBSS containing 1 mg/mL Collagenase D
854 (Roche, 11088882001) and 50 U/mL DNase I for 30 minutes at 37°C to facilitate cell dissociation.
855 The resulting cell suspension was then washed with cold HBSS and centrifuged at 600 x g for 10
856 minutes at 4°C. The harvested liver was perfused using Liver Perfusion Medium (Gibco,
857 17701038), followed by mincing and enzymatic digestion in Liver Digest Medium (Gibco,

858 17703034) at 37°C for 30 minutes. The digested liver tissue was then pressed through a 70 μm
859 strainer into HBSS. The resulting cell suspension was centrifuged at 50 g for 3 minutes to separate
860 the hepatocyte-enriched pellet, which was discarded. The supernatant, containing non-parenchymal
861 cells, was further centrifuged at 700 g for 15 minutes at 4°C. The resulting cell pellet was
862 resuspended in a solution of 5 mL PBS with 0.5% BSA and 5 mL of 50% Percoll (Cytiva, 17-0891-
863 01) diluted in PBS. This suspension underwent Percoll gradient centrifugation at 700 g for 30
864 minutes at 20°C to enrich specific cell populations. The peritoneal cavity was lavaged with HBSS
865 to collect peritoneal fluid. The retrieved fluid was then passed through a 70 μm strainer to remove
866 debris, followed by centrifugation at 600 x g for 10 minutes at 4°C to pellet the peritoneal cells.
867 Blood was collected via cardiac puncture into a heparin-coated tube. The cells were separated by
868 centrifugation at 400 g for 10 minutes at 4°C following a wash with HBSS. RBCs present in a
869 single-cell suspension were lysed using 1X RBC Lysis buffer (BioLegend, 420302) for 3 minutes
870 at room temperature. However, this step was excluded when analyzing erythroid cells and RBCs.
871 Following that, the cells were washed with 1X HBSS and centrifuged at 600g for 10 minutes at
872 4°C. The resulting pellet was processed for subsequent functional assays and antibody labeling.

873 **Generation of iRPMs**

874 Mononuclear cells were aseptically harvested from the femurs and tibias of mice and subsequently
875 cultured at a concentration of 0.5 X 10^6/1mL in RPMI-1640 medium (Gibco, 61870036)
876 supplemented with 10% FBS (Cytiva, SV30160.03), 1X Penicillin-Streptomycin (Gibco,
877 15140122), and 20 ng/mL of macrophage colony-stimulating factor (MCSF, BioLegend, 576406)
878 in a 5% CO_2 incubator at 37°C. On days 4 and 6 of culture, the medium was replaced with fresh
879 complete medium supplemented with 20 μM hemin (Sigma-Aldrich, 51280) and 10 ng/mL
880 interleukin-33 (IL-33) (BioLegend, 580506). All subsequent experiments were performed on day
881 8 of culture. For treatments, hemin (Sigma-Aldrich, 51280) solution was prepared with 0.15 M
882 NaCl containing 10% NH_4OH. For the phagocytosis assay, iRPMs were treated for 1 hour with 10
883 μM Entospletinib (Selleck, S7523), 15 hours with 10μM ERG240 (MedChemExpress, HY-
884 W193545A), 15 hours with 10μM BAY-069 (MedChemExpress, HY-148242), 15 hours with 10
885 mM leucine (Sigma-Aldrich, L8000), 24 hours with 100 μM deferoxamine (DFE, Sigma-Aldrich,
886 D9533), 30 minutes with 10 μM BAPTA/AM (CALBIOCHEM, 196419), 1 hour with 3 mM EGTA
887 (Sigma, E8145), 16 hours with 2.5 μM STO609 (Sigma-Aldrich, S1318), 30 minutes with 20 μM
888 W7 (Sigma-Aldrich, 681629), 30 minutes with 5U/ml apyrase (Sigma-Aldrich, A6535), 30 minutes

889 with 25 μM EIPA (Selleckchem, S9849), 1 hour with 10 μM BisindolylmaleimideI (Sigma-
890 Aldrich, 203290), 30 minutes with 100 μM Piceatannol (Sigma-Aldrich, P0453). Vamifeport was
891 a kind gift from CSL Vifor and was purchased from MedChem Express (VIT-2763), and was used
892 for 15 hours at 20 μM concentration.

893 **Flow Cytometric Analysis and Cell Sorting**

894 Cell suspensions of spleens and livers at a concentration of approximately 1×10^7, along with
895 iRPMs, were stained with LIVE/DEAD Fixable Aqua/Violet (Invitrogen, L34966/L34964)
896 following the manufacturer's instructions to identify dead cells. After extensive washing, Fc block
897 was added to the cells at a 1:100 dilution in FACS buffer and incubated at 4˚C for 10 minutes. The
898 cells were then stained with fluorophore-conjugated antibodies at a dilution of 1:100 to 1:400,
899 depending on the titration, in FACS buffer for 30 minutes at 4˚C. The cells were washed thoroughly
900 with FACS buffer and analyzed using flow cytometry. For the analysis of splenic RPM populations,
901 surface antibodies such as CD45 (Biolegend, 30-F11), CD45R/B220 (Biolegend, RA3-6B2), Ly-
902 6G/Ly-6C (Gr-1) (Biolegend, RB6-8C5), CD3 (Biolegend, 17A2), F4/80 (Biolegend, BM8),
903 CD11b (Biolegend, M1/70), and TREML4 (Biolegend, 16E5) were used. For erythroid cell
904 analysis, TER-119 (Biolegend) and CD71 (Biolegend, RI7217) were included. Staining for
905 proteins linked to amino acid and lipid metabolism utilized antibodies against BCKDHB (Santa
906 Cruz Biotechnology, sc-374630), SLC7A7 (Invitrogen, PA5-113527), CPT2 (Novus Biologicals,
907 NBP1-85471), ACADSB (Proteintech, 13122-1-AP), ABHD12B (Proteintech, 20623-1-AP),
908 citrate synthase (Proteintech, 16131-1-AP), and DGAT1 (Novus Biologicals, NB110-41487). The
909 analysis of liver KCs and iRPM populations involved the use of surface antibodies, including CD45
910 (Biolegend, 30-F11), F4/80 (Biolegend, BM8), and CD11b (Biolegend, M1/70). FPN detection
911 was performed using a non-commercial antibody that recognizes the extracellular loop of mouse
912 FPN (rat monoclonal, Amgen, clone 1C7) directly conjugated with Alexa488 (Alexa Fluor 488
913 Labeling Kit ab236553). To analyze RBCs, surface antibodies such as CD45 (Biolegend, 30-F11),
914 TER-119 (Biolegend), and CD71 (Biolegend, RI7217) were used. Lastly, the analysis of peritoneal
915 macrophages involved the use of surface antibodies, including CD45 (Biolegend, 30-F11), F4/80
916 (Biolegend, BM8), MHCII (Biolegend, M5/114.15.2), and CD11b (Biolegend, M1/70). Events
917 were acquired using Aria II (BD Biosciences) or CytoFLEX (Beckman Coulter) and were analyzed
918 using FlowJo or CytExpert, respectively. For RNA sequencing (RNA-seq) and ATP levels

919 quantification, RPMs were sorted into Trizol-LS (Invitrogen, 10296010) or assay buffer,
920 respectively, using an Aria II cell sorter (BD Biosciences) with an 85 µm nozzle.

921 **Functional Assays and Detection of Intracellular Fe^{2+} Iron**

922 To assess intracellular ROS levels, CellROX Deep Red Reagent (Invitrogen, C10422) was used,
923 and fluorescence was measured in the APC channel following the manufacturer's protocol. The
924 lysosomal activity was evaluated using the Lysosomal Intracellular Activity Assay Kit (Biovision,
925 K448) and fluorescence was measured in the FITC channel as directed by the manufacturer. To
926 measure mitochondrial activity, the tetramethylrhodamine ethyl ester (TMRE) fluorescent probe
927 (Sigma-Aldrich, 87917) was utilized at a concentration of 400 nM for 30 min at 37 °C, and the
928 fluorescence was measured in the PE channel. Mitochondrial mass was measured by fluorescence
929 levels upon staining with MitoTracker Green (Invitrogen, M7514) at 100 nM for 30 min at 37 °C
930 in the FITC channel. Calcium (Ca^{2+}) levels (FITC channel) were determined by using Cal-520 AM
931 probe (Abcam, ab171868) at 5 µM for 1 hour at room temperature. The intracellular ferrous iron
932 (Fe^{2+}) content was determined using FerroOrange (Dojindo, F374) through flow cytometric
933 analysis in the PE channel. Lipid droplet content was quantified using the Lipid Droplet Assay Kit
934 Deep Red (Dojindo, LD06-10) following the manufacturer’s protocol, with fluorescence recorded
935 in the APC channel. The cells were surface-stained and incubated with 1 µM FerroOrange dye in
936 HBSS for 30 min at 37 °C. The analysis was performed directly via flow cytometry without further
937 washing, as previously described. Glucose uptake was measured using the Glucose Uptake
938 Capacity Assay Kit (Dojindo, UP03), and fluorescence was measured in the APC channel as per
939 the manufacturer's protocol. To perform intracellular staining, cells that had already been surface-
940 stained were fixed using 4% PFA and permeabilized with 0.5% Triton-X in PBS. The cells were
941 then stained with appropriate primary antibodies for 1 hr at 4°C, followed by a 30-minute
942 incubation with Alexa Fluor 488 or Alexa Fluor 647 conjugated anti-Rabbit IgG (1:1000 Thermo
943 Fisher, A-21206). Afterward, the geometric mean fluorescence intensities (MFI) of the
944 probes/target protein levels were measured by flow cytometry using Aria II (BD Biosciences) or
945 CytoFLEX (Beckman Coulter). Data were then analyzed using FlowJo or CytExpert software,
946 respectively. For the probes that emitted in PE, TREML4 was excluded, and RPMs were gated as
947 F4/80^{high} CD11b^{dim}. The MFI of the adequate fluorescence minus one (FMO) control was
948 subtracted from the samples' MFI to quantify the data. The data were further normalized for
949 analysis.

950 **ATP levels**

951 The levels of cellular ATP in FACS-sorted RPMs (10000 cells per sample) were measured using
952 the ATP Assay Kit (Sigma-Aldrich, MAK473) according to the manufacturer's instructions.

953 **Magnetic Sorting of RPMs**

954 60 x 10^6 cells were incubated for 15 minutes at 4°C in PBS containing 5% Normal Rat Serum
955 (Thermo Scientific, 10710C) and anti-CD16/32 antibody (Biolegend, 101320) in a 5 mL round-
956 bottom tube. The cells were then labeled with anti-F4/80 (APC, Biolegend, 123116), anti-Ly-
957 6G/Ly-6C (Gr-1) (Biotin, Biolegend, 108403), anti-CD3 (Biotin, Biolegend, 100243), anti-mouse
958 Ly-6C (Biotin, Biolegend, 128003), and anti-B220 (Biotin, Biolegend, 103204) for 20 minutes at
959 4°C in the dark. The cells were washed with a cold PBS solution containing 2 mM EDTA and 0.5%
960 BSA (hereafter referred to as "sorting buffer") and centrifuged at 600 g for 10 minutes. The pellet
961 was resuspended in 400 µL of sorting buffer containing 50 µL of MojoSort Streptavidin Nanobeads
962 (Biolegend, 480016) and kept in the cold and dark for 15 minutes. After incubation, an additional
963 400 µL of sorting buffer was added to the cells, and the tube was placed on an EasyEights EasySep
964 Magnet (STEMCELL, 18103) for 7 minutes. The supernatant was transferred to a fresh 5 mL tube
965 and centrifuged at 600 g for 10 minutes. The pellet was resuspended in 100 µL of sorting buffer,
966 and 10 µL of MojoSort Mouse anti-APC Nanobeads (Biolegend, 480072) were added. The
967 suspension was gently pipetted and incubated for 15 minutes at 4°C in the dark. The tube was then
968 placed on a magnet for 7 minutes, and the supernatant was saved for analysis. The beads with
969 attached F4/80+ cells were washed with sorting buffer and counted under a light microscope with
970 a Neubauer chamber. The cells were pelleted and frozen in liquid nitrogen for further analysis.

971 **Magnetic Sorting of T Cells, B Cells, Granulocytes, Peritoneal Macrophages, and Kupffer**
972 **Cells**

973 Magnetic sorting of splenic T cells, B cells, and granulocytes was performed using the same general
974 workflow as described for splenic RPM isolation, with modified antibody labeling and bead
975 combinations. Briefly, cells were Fc-blocked and stained with biotinylated antibodies against B220
976 and Gr-1, a PE-conjugated antibody against CD3, and an APC-conjugated antibody against F4/80.
977 Biotin-labeled B cells and granulocytes were isolated using streptavidin nanobeads, $CD3^+$ T cells
978 were isolated using anti-PE nanobeads, and $F4/80^+$ macrophages were positively selected using
979 anti-APC nanobeads. This approach yielded purified $CD3^+$ T cells as well as B-cell and granulocyte

980 fractions for further analysis. Peritoneal macrophages were isolated using the same marker and
981 bead strategy as splenic macrophages, with biotinylated antibodies against CD3, B220, and Gr-1
982 for lineage depletion, followed by positive selection of F4/80^{+} cells using anti-APC nanobeads.

983 Magnetic sorting of Kupffer cells was performed according to a two-step liver perfusion protocol
984 with minor modifications. Briefly, mice were euthanized, and livers were perfused in situ through
985 the inferior vena cava with Liver Perfusion Medium for 3 min, followed by perfusion with
986 prewarmed Liver Digest Medium for 15–20 min after transection of the portal vein. Digested livers
987 were gently dissociated in RPMI 1640, filtered through a 100-µm strainer, and subjected to two
988 rounds of low-speed centrifugation (50 g, 3 min) to remove hepatocytes. The resulting non-
989 parenchymal cell fraction was centrifuged at 650 g for 15 min at 4 °C, treated with red blood cell
990 lysis buffer, and further purified using a two-layer Percoll gradient. Cells collected from the
991 interphase between 25% and 50% Percoll were washed, Fc-blocked, and incubated with anti-F4/80
992 MicroBeads UltraPure. F4/80^{+} Kupffer cells were isolated using magnetized LS separation
993 columns, washed, and prepared for downstream analyses. All cell isolations were performed at 4
994 °C, and purified cells were counted, pelleted, and snap-frozen in liquid nitrogen prior to
995 intracellular BCAA quantification.

996 **Measurement of Cellular Iron Levels**

997 To determine the levels of total iron in magnetically sorted RPMs, the Iron Assay Kit from Sigma-
998 Aldrich (MAK025) was employed by following the manufacturer's instructions. The volume of
999 buffers and reagents used in the measurement of total iron in RPMs was adjusted accordingly. The
1000 absorbance at 593 nm was recorded using a Nanodrop ND-1000 Spectrophotometer from Thermo
1001 Fisher Scientific. Iron concentrations in RPMs (ng/µL) were calculated from the standard curve
1002 and then normalized to the number of cells in each sample.

1003 ***In Vivo* RBC Lifespan**

1004 A sterile solution of EZ-Link Sulfo-NHS Biotin (Thermo Fisher Scientific, 21217) was prepared
1005 in PBS with a final concentration of 1 mg per 100 µL. The solution was then filtered through a 0.1
1006 µm filter (Millipore, SLVV033RS). One day before the first blood collection, 100 µL of the sterile
1007 Biotin solution was intravenously injected into the mice. Blood samples were collected from the
1008 tail vein on days 0, 4, 11, 18, and 25, using heparinized capillaries to prevent clotting. RBCs were
1009 separated by centrifugation at 400 g for 5 minutes at 4°C, and each sample was resuspended in 250

1010 μL of HBSS containing 5% normal rat serum (Thermo Fisher Scientific). The suspension was then
1011 mixed with 2 μL of fluorescently labeled anti-TER-119 and streptavidin, except for the
1012 fluorescence minus one (FMO) sample in each group, where fluorescent streptavidin was omitted.
1013 After incubation at 4°C for 30 minutes, the samples were centrifuged and resuspended in HBSS.
1014 Flow cytometry was used to determine the percentage of biotinylated erythrocytes.

1015 **Preparation of Stressed RBCs for Erythrophagocytosis Assays**

1016 The preparation and staining of stressed RBCs followed a previously outlined procedure. To obtain
1017 the RBCs, mice were humanely euthanized, and whole blood was aseptically collected via cardiac
1018 puncture into CPDA-1 solution (Sigma-Aldrich, C4431) with a final concentration of 10%. The
1019 collected whole blood was combined, and plasma was separated by centrifugation at 400 g for 15
1020 min at 4°C, then filtered through a 0.1 μm filter and stored at 4°C. The RBCs were then suspended
1021 in HBSS, and leukocytes were eliminated using Lymphosep (Biowest, L0560-500). Following this,
1022 the cells were subjected to a 30-minute heating period at 48°C with continuous agitation to generate
1023 stressed RBCs. To stain the sRBCs, 1×10^{10} RBCs were resuspended in 1 ml of diluent C and mixed
1024 with 1 ml of diluent C containing 4 μM of PKH-67 (Sigma-Aldrich, MINI67) or PKH-26 (Sigma-
1025 Aldrich, MINI26). The mixture was then incubated in the dark for 5 min at 37°C, and the reaction
1026 was stopped by adding 10 mL of HBSS containing 2% FCS and 0.5% BSA. Staining was followed
1027 by two washing steps with HBSS. For *in vitro* EP assays, the cells were resuspended in RPMI-1640
1028 and counted. For the *in vivo* approach, RBCs were resuspended to 50% hematocrit in previously
1029 collected and filtered plasma.

1030

1031 ***In Vitro* Erythrophagocytosis**

1032 On the 8th day post-seeding, stained, and counted sRBCs were added to iRPMs on 12-well plates
1033 in 10-fold excess for 1.5 hours at 37 °C and 5% CO_2. After incubation, the cells were extensively
1034 washed with cold HBSS to eliminate any non-engulfed sRBCs. Subsequently, the cells were
1035 detached using Accutase (BioLegend, 423201), which were then transferred to a round-bottom
1036 FACS tube, washed with HBSS, and centrifuged at 600 g for 5 minutes. The cells were labeled
1037 with antibodies and analyzed using flow cytometry. For time-lapse confocal imaging of the
1038 execution of RBC uptake by iRPMS, sRBCs were stained with pH-sensitive pHrodo™ Deep Red
1039 Mammalian and Bacterial Cell Labeling Kit. The imaging was performed using the Opera Phenix

1040 (PerkinElmer), an automated confocal spinning disk microscope. Imaging was conducted for 120
1041 min, with acquisition every 1.3 min.

1042 ***In Vivo* Erythrophagocytosis**

1043 The mice were intravenously transfused with 100 μL of RBCs resuspended in plasma to 50%
1044 hematocrit. The animals were kept in cages with ad libitum access to food and water for 1.5 hours
1045 before being sacrificed for organ isolation.

1046 **Mini-Hepcidin (PR73) Preparation**

1047 An optimized protocol was developed for preparing mini-Hepcidin (PR73, a kind gift from
1048 Elizabeta Nemeth, UCLA, USA) for intraperitoneal injection in mice. Commercially available
1049 PR73 powder may not represent the pure peptide, so we adjusted the preparation based on the
1050 estimated active component content (80%). The process began by precisely weighing the PR73
1051 powder to account for the estimated 80% active component. This powder was then dissolved in
1052 80% ethanol to ensure complete extraction of the peptide. The solution was thoroughly mixed using
1053 a vortex mixer to achieve a homogenous suspension. Next, the solution was carefully transferred
1054 to a sterile, low-bind vial (SL-220) to minimize potential losses due to adsorption during
1055 incubation. A brief heat treatment at 37°C for a few seconds facilitated the complete dissolution of
1056 any undissolved particles. Following the heat treatment, the vial cap was removed, and the solution
1057 was aliquoted into designated culture tubes for individual injections. A Speedvac concentrator was
1058 then used to evaporate the ethanol, resulting in a concentrated PR73 gel within each tube. To
1059 achieve a final working concentration of 0.5 nmol/μl, 2 ml of sterile, injectable-grade water was
1060 added to each tube containing the PR73 gel. The tubes were vigorously vortexed to ensure complete
1061 dissolution of the gel and homogenization of the solution. For *in vivo* experiments, 100 μl of the
1062 prepared PR73 stock solution was administered per mouse via intraperitoneal injection. A solvent
1063 control solution was prepared by following the same steps outlined above but substituting the PR73
1064 solution with only 80% ethanol. This control solution served as a baseline for comparison with the
1065 PR73-treated mice in subsequent experiments.

1066 **Live-Cell Imaging of Erythrophagocytosis in iRPMs**

1067 To assess erythrophagocytic capacity, iRPMs were seeded in Greiner Bio-One CELLSTAR
1068 μClear™ 96-well, Cell Culture-Treated, Flat-Bottom Microplate and cultured with IB versus ID
1069 serum. iRPMs with ID serum were treated with PR73 for 4 hours. Following PR73 treatment,

1070 iRPMs were exposed to temperature-stressed, pHrodo-labeled RBCs, prepared using the pHrodo™
1071 Deep Red Mammalian and Bacterial Cell Labeling Kit (Thermo Fisher Scientific). The stressed
1072 and labeled RBCs were added to the wells, and the plate was immediately transferred to the Opera
1073 Phenix™ High-Content Screening System (PerkinElmer), maintained at 37°C with 5% CO_2. Live-
1074 cell imaging was performed for 2 hours with images captured at regular intervals to monitor the
1075 uptake of RBCs, and data were analyzed using Harmony High-Content Imaging and Analysis
1076 Software (PerkinElmer).

1077 **BCAA levels**

1078 Intracellular branched-chain amino acid content was quantified in magnetically sorted $CD3^+$ T
1079 cells, B220+ B cells, together with GR1+ granulocytes, RPMs, peritoneal macrophages, and
1080 Kupffer cells, using the Branched Chain Amino Acid Assay Kit (Sigma-Aldrich, MAK003)
1081 following the manufacturer's instructions.

1082 **Metabolic Flux Seahorse Assay**

1083 Metabolic flux was assessed using a Seahorse XF-96 Extracellular Flux Analyzer (Agilent
1084 Technologies) Mito Stress Test (Agilent,103010-100). Magnetically sorted RPMs (8×10^4
1085 cells/well) from IB and ID mice were plated onto poly-L-lysine-coated Seahorse XF HS Miniplates
1086 (Agilent, 103725-100). Cells were incubated in Seahorse XF RPMI medium (Agilent, 103576-100)
1087 supplemented with 2 mM L-glutamine (Agilent, 103579-100), 1 mM sodium pyruvate (Agilent,
1088 103578-100), and 25 mM glucose (pH adjusted to 7.4; Agilent 103577-100) at 37°C in a non-CO_2
1089 incubator for 60 minutes. Real-time oxygen consumption rate (OCR) was measured under basal
1090 conditions and following sequential injections of 1 μM oligomycin, 1 μM FCCP, and a mixture of
1091 1 μM rotenone and 1 μM antimycin A.

1092 **Mitochondrial substrate utilization (MitoPlate) Assay**

1093 Mitochondrial substrate utilization was assessed using the MitoPlate S-1 assay (Biolog, 14105)
1094 according to the manufacturer's protocol. Magnetically sorted RPMs from IB, ID, and ID+ERG240
1095 mice were pooled (four mice per condition), counted, and resuspended in MitoPlate assay medium
1096 before seeding at 8×10^4 cells per well onto the precoated 96-well Mitoplates, containing the dye
1097 mix MC. Plates were loaded into a Tecan Infinite 200 Pro maintained at 37°C, and kinetic OD_{590}
1098 measurements were collected every 10 minutes throughout the assay. Absolute blank-corrected
1099 OD values from the 6-hour time point were used for analysis.

1100 **Voluntary Oral Drug Administration**

1101 Strawberry-flavored gelatin jellies were prepared under sterile conditions in 96-well plates (100
1102 µL/well), with or without ENTO and ERG240. Gelatin (8% w/v, Sigma-Aldrich, G9391) was
1103 dissolved in warm, sterile water, and strawberry flavoring essence (1% v/v, OstroVit,
1104 5903933916217) was added. Just before gelation, ENTO or ERG240 was added to the appropriate
1105 wells of a sterile 96-well plate to achieve the desired final concentration, while control wells
1106 received vehicle only. The gelatin solution (100 µL) was then added to each well, and the plates
1107 were refrigerated at 4°C until solid. To acclimate IB and ID mice, two drug-free jellies were
1108 provided per cage daily for 2-3 days (two mice per cage). This co-housing approach minimized
1109 stress associated with individual training. Following acclimation, mice readily consumed the jellies
1110 within 15-20 minutes. Drug-containing jellies were administered at approximately the same time
1111 each day for two or three weeks.

1112 **Generation of Ferroportin Overexpressing iRPMs**

1113 We successfully cloned the wild-type *Slc40a1* gene, encoding mouse ferroportin (FPN; Uniport
1114 ID: Q9JHI9), into the HIV SFFV lentiviral vector. Lentiviral production involved transfecting the
1115 chosen lentiviral vectors (FPN or Mock) along with the psPAX2 packaging vector and the pMD2.G
1116 envelope vector into HEK293T cells. The resulting viral supernatants were harvested and titrated
1117 to determine viral concentration. Subsequently, iRPMs were transduced on Day 1 with lentiviral
1118 vectors at a multiplicity of infection (MOI) of 1. On Days 4 and 6, the culture medium was replaced
1119 with fresh complete medium supplemented with 20 µM hemin and 10 ng/mL interleukin-33 (IL-
1120 33). This MOI ensured efficient transduction while minimizing potential cytotoxicity. Expression
1121 levels of surface FPN were measured in each experiment using flow cytometry. This verification
1122 step confirmed successful FPN overexpression in iRPM population, allowing for functional
1123 analysis of the consequences in subsequent experiments.

1124 **Hepcidin Measurement with ELISA**

1125 Serum hepcidin levels were measured using the Hepcidin-Murine Compete ELISA Kit (Intrinsic
1126 LifeSciences, HMC-001) following the manufacturer's instructions. Optical density was
1127 determined with a microplate reader at a wavelength of 450 nm.

1128 **Erythropoietin (EPO) Measurement with ELISA**

1129 Serum EPO levels were measured using the Mouse Erythropoietin/EPO Quantikine ELISA Kit
1130 (R&D Systems, MEP00B) following the manufacturer's instructions. Optical density was
1131 determined with a microplate reader at a wavelength of 450 nm.

1132 **Transferrin Saturation and Tissue Iron Measurements**

1133 The levels of serum iron and unsaturated iron-binding capacity were quantified using SFBC
1134 (Biolabo, 80008) and UIBC (Biolabo, 97408) kits per the manufacturer's instructions. Transferrin
1135 saturation was determined using the formula SFBC/(SFBC+UIBC) x 100. Tissue non-heme iron
1136 content was measured using the bathophenanthroline method, and the results were calculated based
1137 on tissue dry weight, as previously described[83].

1138 **RT-qPCR**

1139 RNA from cell pellets was isolated using an RNA purification kit (Eurex) according to the
1140 manufacturer's instructions. RNA from liver, heart and kidney tissues was isolated using TRIzol™
1141 reagent according to the manufacturer's instructions. 400 ng of RNA was subjected to reverse
1142 transcription. In the first stage of the reaction, RNA was denatured, and random primers were
1143 attached. For this purpose, a mixture consisting of 400 ng RNA, 1 µL of random primers at a
1144 concentration of 200 ng/µL, and nuclease-free water was prepared so that the total reaction volume
1145 was 17.7 µL. The mixture was incubated at 70°C for 10 minutes and then cooled to 4°C. The next
1146 step was to add the reaction mixture to the tubes, which contained: 0.3 µl RevertAid H Minus
1147 reverse transcriptase, 1 µL of 10 mM dNTP solution, and 5 µL of reaction buffer. The total reaction
1148 volume was 25 µL. The reaction was carried out for 60 minutes at 42°C, 70°C, 10 minutes. The
1149 obtained cDNA was diluted 9x and then used for quantitative polymerase chain reaction (qPCR).
1150 The reaction mixture consisted of 4 µL cDNA, 7.5 µL SG qPCR Master Mix (2x), and 1.5 µL of a
1151 5 µM solution of forward and reverse primers. The whole was supplemented with nuclease-free
1152 water to a final reaction volume of 15 µL. The qPCR reaction was carried out using the LightCycler
1153 96 Real-Time PCR System (Roche). The reaction was pre-incubated at 95°C for 600 s, and then
1154 two-step amplification was performed 40x (95°C x 15 s, 60°C x 60 s).

1155 **Immunohistochemistry of Spleen Tissues**

1156 The spleen was fixed in 4% PFA at 4°C for 24 h. Tissues were washed with PBS (3x30min) and
1157 incubated for 2 h in 12.5% and then in 25% sucrose solution for 48 h. Subsequently, spleen tissue
1158 fragments were embedded in the Cryomatrix medium, frozen in liquid nitrogen, and cut into 10 µm

1159 thick sections using a cryo microtome (Leica). The sections were mounted on glass slides and
1160 stored at -20°C. Before staining, the sections were warmed at room temperature for 30 min, and
1161 then their edges were surrounded using a Pap Pen Liquid Blocker. Next, the slides with sections
1162 were washed in PBS for 10 min and permeabilized in 0.1% Triton X-100 solution for 20 min.
1163 Nonspecific antibody binding was blocked by incubating the sections in 3% BSA solution for 1 h
1164 at room temperature. To visualize RPMs, the tissues were incubated with FITC-conjugated F4/80
1165 antibody (1:100), and for FPN, with Alexa Fluor 647-conjugated FPN antibody (1:100) in 3% BSA
1166 for 2 h at room temperature in the dark. After incubation with antibodies, the tissues were washed
1167 5 x 5 min in 0.1% Triton X-100 solution to remove unbound antibodies. To stain cell nuclei, the
1168 sections were incubated with Hoechst 33342 diluted in 0.1% Triton X-100 solution (final
1169 concentration 1 μg/ml) for 10 min at room temperature in the dark. Then, the sections were washed
1170 for 3 x 5 min in 0.1% Triton X-100 solution, incubated in PBS for 10 min, and mounted with a
1171 coverslip using ProLong™ Glass Antifade Mountant. Samples were imaged on a confocal
1172 microscope with a Plan-Apochromat 40x/1.3 NA oil immersion objective (Zeiss) LSM 800.

1173 **Histological and Histochemical Analysis**

1174 Following fixation in 10% formalin for 24 h, spleens were stored in 70% ethanol before further
1175 preparation. The tissue was embedded in paraffin and 7 μm cross-sections were cut with a
1176 microtome (Reichert-Jung, Germany). Sections were prepared as described above. After mounting
1177 on glass slides, sections were deparaffinized, incubated with a working solution containing Perls'
1178 Prussian Blue for 30 min, counterstained with pararosaniline solution for 2 min, and analyzed under
1179 standard light microscopy (Olympus CH2).

1180 **Transcriptome analysis by RNA-seq**

1181 RNA-seq libraries were generated from FACS-sorted RPMs (minimum 100,000 cells per sample)
1182 using the Smart-seq2 protocol84, which is optimized for low-input total mRNA sequencing. RNA
1183 integrity and library quality were checked by a Bioanalyzer. Sequencing was performed on an
1184 Illumina NextSeq500 platform, producing 75-bp single-end reads at ~50 million reads per sample.
1185 RNA-seq was carried out at the EMBL GeneCore facility (Heidelberg, Germany). Sequence reads
1186 were trimmed to remove possible adapter sequences and nucleotides with poor quality using
1187 Trimmomatic v.0.36. The trimmed reads were mapped to the Mus musculus GRCm38 reference
1188 genome available on ENSEMBL using the STAR aligner v.2.5.2b. Unique gene hit counts were

1189 calculated by using featureCounts from the Subread package v.1.5.2. Normalization and differential
1190 expression analysis were performed using DESeq2. The Wald test was used to generate p-values
1191 and log2 fold changes. Genes with an adjusted p-value < 0.05 and absolute log2 fold change > 1
1192 were called as differentially expressed genes.

1193 **Proteomic analysis of RPMs**

1194 Sample Preparation. Magnetically isolated RPMs were obtained from the spleens of IB and ID
1195 female C57BL/6J mice. The cells were lysed using RIPA buffer. Proteins were precipitated using a
1196 chloroform/methanol method, washed with methanol, and reconstituted in 100 mM HEPES (pH
1197 8.0) containing 10 mM TCEP and 10 mM chloroacetamide.

1198 LC-MS/MS Analysis. 10 µg of each lysate was subjected to an in-solution tryptic digest using a
1199 modified version of the Single-Pot Solid-Phase-enhanced Sample Preparation (SP3) protocol[85,86].
1200 To this end, lysates were added to Sera-Mag Beads (Thermo Scientific, #4515-2105-050250, 6515-
1201 2105-050250) in 10 µl 15% formic acid and 30 µl of ethanol. The binding of proteins was achieved
1202 by shaking for 15 min at room temperature. SDS was removed by 4 subsequent washes with 200
1203 µl of 70% ethanol. Proteins were digested overnight at room temperature with 0.4 µg of sequencing
1204 grade modified trypsin (Promega, V5111) in 40 µl Hepes/NaOH, pH 8.4 in the presence of 1.25
1205 mM TCEP and 5 mM chloroacetamide (Sigma-Aldrich, C0267). Beads were separated and washed
1206 with 10 µl of an aqueous solution of 2% DMSO, and the combined eluates were dried down.

1207 Up to 10 µg of peptides per sample were labeled with TMT10plex™ reagents following established
1208 protocols[87]. Briefly, 0.8 mg of TMT reagent was dissolved in 45 µL of anhydrous acetonitrile, and
1209 4 µL of this solution was added to each peptide sample. Labeling was carried out at room
1210 temperature for 1 hour. The reaction was quenched by adding 4 µL of 5% hydroxylamine in water,
1211 followed by a 15-minute incubation at room temperature. Labeled peptides were pooled for
1212 multiplexing, desalted using an Oasis® HLB µElution Plate (Waters #186001828BA) according to
1213 the manufacturer's instructions, and dried by vacuum centrifugation.

1214 Offline high-pH reversed-phase fractionation was performed as described previously[88], using an
1215 Agilent 1200 Infinity HPLC system equipped with a Gemini C18 analytical column (3 µm particle
1216 size, 110 Å pore size, 100 × 1.0 mm; Phenomenex) and a matching Gemini C18 SecurityGuard pre-
1217 column (4 × 2.0 mm; Phenomenex). Peptides were separated at a flow rate of 0.1 mL/min using
1218 mobile phase A (20 mM ammonium formate, pH 10.0) and mobile phase B (100% acetonitrile).

1219 The chromatographic gradient was as follows: 100% A for 2 min, linear increase to 35% B over
1220 59 min, ramp to 85% B in 1 min, held at 85% B for 15 min, followed by re-equilibration at 100%
1221 A for 13 min. A total of 48 fractions were collected and subsequently pooled into 12 final fractions.
1222 Nanoflow LC-MS/MS analysis was performed on an UltiMate 3000 RSLCnano system (Thermo
1223 Fisher Scientific) coupled to an Orbitrap Fusion™ Lumos™ Tribrid™ mass spectrometer (Thermo
1224 Fisher Scientific). Peptides were initially loaded onto a µ-Precolumn C18 PepMap™ 100 trap
1225 cartridge (300 µm i.d. × 5 mm, 5 µm particles, 100 Å; Thermo) at 30 µL/min with 0.05% TFA in
1226 water for 6 min. Analytical separation was carried out using a nanoEase™ M/Z HSS T3 column
1227 (75 µm i.d. × 250 mm, 1.8 µm particles, 100 Å; Waters), equilibrated with solvent A (3% DMSO,
1228 0.1% formic acid in water). Peptides were eluted at 0.3 µL/min using a gradient of solvent B (3%
1229 DMSO, 0.1% formic acid in acetonitrile) as follows: 2–8% B over 6 min, 8–25% over 99 min, 25–
1230 40% over 5 min, ramp to 85% in 0.1 min, held at 85% for 3.9 min, followed by re-equilibration to
1231 2% B for 6 min. Mass spectrometry was performed using a Pico-Tip emitter (360 µm OD × 20 µm
1232 ID, 10 µm tip; CoAnn Technologies) with a spray voltage of 2.4 kV and a capillary temperature of
1233 275 °C. Full MS scans were acquired in the Orbitrap at a resolution of 120,000 (at m/z 200), over
1234 a mass range of m/z 375–1,500, with an AGC target set to 'standard' and a maximum injection time
1235 of 50 ms. The instrument operated in data-dependent acquisition (DDA) mode. MS/MS spectra
1236 were acquired in the Orbitrap at a resolution of 30,000, with a maximum injection time of 94 ms
1237 and an AGC target of 200%. Precursors were fragmented using higher-energy collisional
1238 dissociation (HCD) at 36% normalized collision energy. A quadrupole isolation window of 0.7 m/z
1239 was used, with dynamic exclusion set to 60 s. Only precursor ions with charge states between 2
1240 and 7 were selected for fragmentation.

1241 Acquired data were analyzed using IsobarQuant and Mascot V2.4 (Matrix Science) using a reverse
1242 UniProt FASTA Mus musculus database (UP000000589) including common contaminants. The
1243 following modifications were considered: Carbamidomethyl (C, fixed), TMT10plex (K, fixed),
1244 Acetyl (N-term, variable), Oxidation (M, variable), and TMT10plex (N-term, variable). The mass
1245 error tolerance for full scan MS spectra was set to 10 ppm and for MS/MS spectra to 0.02 Da. A
1246 maximum of 2 missed cleavages were allowed. A minimum of 2 unique peptides with a peptide
1247 length of at least seven amino acids and a false discovery rate below 0.01 were required on the
1248 peptide and protein level.

1249 Data Processing. The data were processed using MaxQuant 2.1.3.0, with peptides identified from
1250 MS/MS spectra searched against the Uniprot Mouse Reference Proteome (UP000000589) using
1251 the built-in Andromeda search engine. Fixed modifications included cysteine
1252 carbamidomethylation, while variable modifications included methionine oxidation,
1253 glutamine/asparagine deamination, and protein N-terminal acetylation. In silico digests allowed for
1254 cleavages of arginine or lysine followed by any amino acid (trypsin/P), with up to two missed
1255 cleavages permitted. The false discovery rate (FDR) was set to 0.01 for peptides, proteins, and
1256 sites. Match between runs was enabled, and other parameters were used as preset in the software.
1257 Protein identification and intrasample quantification were performed using the iBAQ algorithm in
1258 MaxQuant.

1259 **Transmission Electron Microscopy (TEM) of the Spleen**

1260 Fresh spleen samples, approximately 3 mm^2 in size, were fixed in 2.5% glutaraldehyde for 24 hours
1261 at 4°C. Following fixation, the samples were washed in PBS and postfixed with 1% osmium
1262 tetroxide for 1 hour. After rinsing with water, the samples were incubated in 1% aqueous uranyl
1263 acetate for 12 hours at 4°C. The samples were then dehydrated at room temperature using
1264 increasing concentrations of ethanol, infiltrated with epoxy resin (Sigma-Aldrich, 45-359-1EA-F),
1265 and polymerized for 48 hours at 60°C. The polymerized resin blocks were trimmed using a tissue
1266 processor (Leica EM TP) and sectioned into ultrathin slices (65 nm thick) with an ultramicrotome
1267 (EM UC7, Leica). These ultrathin sections were collected on nickel grids with 200 mesh (Agar
1268 Scientific, G2200N). The specimen grids were examined with a Tecnai T12 BioTwin transmission
1269 electron microscope (FEI, Hillsboro, OR, USA) equipped with a 16-megapixel TemCam-F416
1270 camera (TVIPS GmbH) at the in-house Microscopy and Cytometry Facility.

1271 **Preparation of Schematic Figures**

1272 The graphical abstract was created in BioRender. Mleczko-Sanecka, K. (2025)
1273 https://BioRender.com/y54j6da.

1274 **Statistical Analysis**

1275 Female mice of the same age were randomly assigned to experimental groups. Samples derived
1276 from mice were collected and assessed/measured randomly, and harvested in a different order
1277 across individual experiments. The sample size, typically ranging from 5 to 9 mice per group or
1278 independent biological cell-based experiments, was determined based on power analysis, prior

experience with similar experiments, and previously published studies in the field of RPM biology. Statistical analysis was conducted using GraphPad Prism (GraphPad Software, Version 9). Data are presented as mean ± SEM unless otherwise noted. Student's t-test with Welch's correction was employed when comparing the two groups. For comparisons involving more than two groups, one-way ANOVA was used, or two-way ANOVA when the simultaneous effects of two factors were being evaluated. Tukey's test was implemented for post-hoc analysis following ANOVA. The following notation was used to indicate statistically significant differences between means: ns for non-significant ($p > 0.05$), * for $p < 0.05$, ** for $p < 0.01$, *** for $p < 0.001$, and **** for $p < 0.0001$.

Data availability

Mass spectrometry proteomics data were deposited to the ProteomeXchange Consortium via the PRIDE partner repository with the dataset identifiers: Project accession: PXD064719 (access secured by a token: lKilHQArXhhB. RNA sequencing data are available in Gene Expression Omnibus GEO under the accession number GSE312948, and metadata were deposited to SRA (PRJNA1274426).

Authorship Contributions

KMS, PKM, RM, KC and PS conceived and planned the experiments; PKM, RM, KC, PS, GZ, MN, AJ, and ML performed research; PKM, RM, KC, PS, GZ, KMS and ML analyzed and visualized data; EN, ZL and FG provided critical reagents/models, KC and KMS curated data; KMS, WP, and EN supervised the study; KC edited the manuscript; PKM, RM and KMS wrote the manuscript.

Conflict of interest

EN is a shareholder and scientific advisor of Intrinsic LifeSciences and Silarus Therapeutics, and a consultant for Disc Medicine, Ionis Pharmaceuticals, Protagonist, GSK and Vifor. Other authors have declared that no conflict of interest exists.

Acknowledgments

We thank the EMBL Proteomics Core Facility (EMBL, Heidelberg) for performing RPM proteomic profiling and data analysis, and the GeneCore team (EMBL, Heidelberg) for performing RNA sequencing. We thank Tara Arvedson (Amgen Inc., USA) for the anti-ferroportin antibody,

Elizabeta Nemeth (UCLA, USA) for PR73, Florent Ginhoux for access to Ms4a3-Cre mice, and Aneta Suwińska for sharing UBI-GFP/BL6 mice, and Vania Manolova (CSL Vifor) for providing vamifeport. Many thanks to Agnieszka Popielska and Anna Kosson, and the staff of the Experimental Medicine Centre (Bialystok, Poland) and Mossakowski Medical Research Institute (Warsaw, Poland) for their technical support. We thank Sylwia Herman for her assistance with the histological analyses and Enrico Tatti for consulting on the MitoPlates profiling data. Mouse-based experiments and animal housing were supported by the Rodent Facility, EM, and Opera Phenix imaging were performed at the Microscopy Facility, and lentiviral DNA constructs were generated at the Genome Engineering Facility of IIMCB (IN-MOL-CELL Infrastructure) funded by the European Union – NextGenerationEU under the National Recovery and Resilience Plan. IN-MOL-CELL Infrastructure was also funded by the European Union under Horizon Europe (Project 101059801 - RACE) and by the RACE-PRIME project carried out within the IRAP programme of the Foundation for Polish Science, co-financed by the European Union under the European Funds for Smart Economy 2021-2027 (FENG). Pratik Kumar Mandal gratefully acknowledges funding from the National Science Centre PRELUDIUM 22 grant, which supported experiments involving lentiviral-mediated FPN overexpression (UMO-2023/49/N/NZ3/04232). This work was funded by the National Science Centre Sonata Bis grant (UMO-2020/38/E/NZ4/00511).

REFERENCES

1. Boada-Romero, E., Martinez, J., Heckmann, B.L., and Green, D.R. (2020). The clearance of dead cells by efferocytosis. Nat Rev Mol Cell Biol *21*, 398–414. https://doi.org/10.1038/s41580-020-0232-1.

2. Doran, A.C., Yurdagul, A., and Tabas, I. (2020). Efferocytosis in health and disease. Nat Rev Immunol *20*, 254–267. https://doi.org/10.1038/s41577-019-0240-6.

3. Moon, B., Yang, S., Moon, H., Lee, J., and Park, D. (2023). After cell death: the molecular machinery of efferocytosis. Exp Mol Med *55*, 1644–1651. https://doi.org/10.1038/s12276-023-01070-5.

4. Sheng, Y.R., Hu, W.T., Chen, S., and Zhu, X.Y. (2024). Efferocytosis by macrophages in physiological and pathological conditions: regulatory pathways and molecular mechanisms. Front Immunol *15*, 1275203. https://doi.org/10.3389/fimmu.2024.1275203.

5. Mukundan, L., Odegaard, J.I., Morel, C.R., Heredia, J.E., Mwangi, J.W., Ricardo-Gonzalez, R.R., Goh, Y.P.S., Eagle, A.R., Dunn, S.E., Awakuni, J.U.H., et al. (2009). PPAR-delta senses and orchestrates clearance of apoptotic cells to promote tolerance. Nat Med *15*, 1266–1272. https://doi.org/10.1038/nm.2048.

6. A-Gonzalez, N., Bensinger, S.J., Hong, C., Beceiro, S., Bradley, M.N., Zelcer, N., Deniz, J., Ramirez, C., Díaz, M., Gallardo, G., et al. (2009). Apoptotic cells promote their own clearance and immune tolerance through activation of the nuclear receptor LXR. Immunity *31*, 245–258. https://doi.org/10.1016/j.immuni.2009.06.018.

7. Mota, A.C., Dominguez, M., Weigert, A., Snodgrass, R.G., Namgaladze, D., and Brüne, B. (2021). Lysosome-Dependent LXR and PPARδ Activation Upon Efferocytosis in Human Macrophages. Front Immunol *12*, 637778. https://doi.org/10.3389/fimmu.2021.637778.

8. Schilperoort, M., Ngai, D., Katerelos, M., Power, D.A., and Tabas, I. (2023). PFKFB2-mediated glycolysis promotes lactate-driven continual efferocytosis by macrophages. Nat Metab *5*, 431–444. https://doi.org/10.1038/s42255-023-00736-8.

9. Morioka, S., Perry, J.S.A., Raymond, M.H., Medina, C.B., Zhu, Y., Zhao, L., Serbulea, V., Onengut-Gumuscu, S., Leitinger, N., Kucenas, S., et al. (2018). Efferocytosis induces a novel SLC program to promote glucose uptake and lactate release. Nature *563*, 714–718. https://doi.org/10.1038/s41586-018-0735-5.

10. Zhang, S., Weinberg, S., DeBerge, M., Gainullina, A., Schipma, M., Kinchen, J.M., Ben-Sahra, I., Gius, D.R., Yvan-Charvet, L., Chandel, N.S., et al. (2019). Efferocytosis Fuels Requirements of Fatty Acid Oxidation and the Electron Transport Chain to Polarize Macrophages for Tissue Repair. Cell Metab *29*, 443-456.e5. https://doi.org/10.1016/j.cmet.2018.12.004.

11. Wang, Y., Subramanian, M., Yurdagul, A., Barbosa-Lorenzi, V.C., Cai, B., de Juan-Sanz, J., Ryan, T.A., Nomura, M., Maxfield, F.R., and Tabas, I. (2017). Mitochondrial Fission Promotes the Continued Clearance of Apoptotic Cells by Macrophages. Cell *171*, 331-345.e22. https://doi.org/10.1016/j.cell.2017.08.041.

12. Jiang, S., Park, D.W., Stigler, W.S., Creighton, J., Ravi, S., Darley-Usmar, V., and Zmijewski, J.W. (2013). Mitochondria and AMP-activated protein kinase-dependent mechanism of efferocytosis. J Biol Chem *288*, 26013–26026. https://doi.org/10.1074/jbc.M113.489468.

13. Tsai, T.-L., Zhou, T.-A., Hsieh, Y.-T., Wang, J.-C., Cheng, H.-K., Huang, C.-H., Tsai, P.-Y., Fan, H.-H., Feng, H.-K., Huang, Y.-C., et al. (2022). Multiomics reveal the central role of pentose phosphate pathway in resident thymic macrophages to cope with efferocytosis-associated stress. Cell Rep *40*, 111065. https://doi.org/10.1016/j.celrep.2022.111065.

14. He, D., Mao, Q., Jia, J., Wang, Z., Liu, Y., Liu, T., Luo, B., and Zhang, Z. (2021). Pentose Phosphate Pathway Regulates Tolerogenic Apoptotic Cell Clearance and Immune Tolerance. Front Immunol *12*, 797091. https://doi.org/10.3389/fimmu.2021.797091.

15. Yurdagul, A., Subramanian, M., Wang, X., Crown, S.B., Ilkayeva, O.R., Darville, L., Kolluru, G.K., Rymond, C.C., Gerlach, B.D., Zheng, Z., et al. (2020). Macrophage Metabolism of Apoptotic Cell-Derived Arginine Promotes Continual Efferocytosis and Resolution of Injury. Cell Metab *31*, 518-533.e10. https://doi.org/10.1016/j.cmet.2020.01.001.

16. Ampomah, P.B., Cai, B., Sukka, S.R., Gerlach, B.D., Yurdagul, A., Wang, X., Kuriakose, G., Darville, L.N.F., Sun, Y., Sidoli, S., et al. (2022). Macrophages use apoptotic cell-derived methionine and DNMT3A during efferocytosis to promote tissue resolution. Nat Metab *4*, 444–457. https://doi.org/10.1038/s42255-022-00551-7.

17. Sukka, S.R., Ampomah, P.B., Darville, L.N.F., Ngai, D., Wang, X., Kuriakose, G., Xiao, Y., Shi, J., Koomen, J.M., McCusker, R.H., et al. (2024). Efferocytosis drives a tryptophan

1384 metabolism pathway in macrophages to promote tissue resolution. Nat Metab *6*, 1736–1755.
1385 https://doi.org/10.1038/s42255-024-01115-7.

1386 18. Merlin, J., Ivanov, S., Dumont, A., Sergushichev, A., Gall, J., Stunault, M., Ayrault, M.,
1387 Vaillant, N., Castiglione, A., Swain, A., et al. (2021). Non-canonical glutamine transamination
1388 sustains efferocytosis by coupling redox buffering to oxidative phosphorylation. Nat Metab *3*,
1389 1313–1326. https://doi.org/10.1038/s42255-021-00471-y.

1390 19. Muckenthaler, M.U., Rivella, S., Hentze, M.W., and Galy, B. (2017). A Red Carpet for Iron
1391 Metabolism. Cell *168*, 344–361. https://doi.org/10.1016/j.cell.2016.12.034.

1392 20. Slusarczyk, P., and Mleczko-Sanecka, K. (2021). The Multiple Facets of Iron Recycling.
1393 Genes (Basel) *12*, 1364. https://doi.org/10.3390/genes12091364.

1394 21. Klei, T.R.L., Meinderts, S.M., van den Berg, T.K., and van Bruggen, R. (2017). From the
1395 Cradle to the Grave: The Role of Macrophages in Erythropoiesis and Erythrophagocytosis. Front
1396 Immunol *8*, 73. https://doi.org/10.3389/fimmu.2017.00073.

1397 22. Kohyama, M., Ise, W., Edelson, B.T., Wilker, P.R., Hildner, K., Mejia, C., Frazier, W.A.,
1398 Murphy, T.L., and Murphy, K.M. (2009). Role for Spi-C in the development of red pulp
1399 macrophages and splenic iron homeostasis. Nature *457*, 318–321.
1400 https://doi.org/10.1038/nature07472.

1401 23. Slusarczyk, P., Mandal, P.K., Zurawska, G., Niklewicz, M., Chouhan, K., Mahadeva, R.,
1402 Jończy, A., Macias, M., Szybinska, A., Cybulska-Lubak, M., et al. (2023). Impaired iron recycling
1403 from erythrocytes is an early hallmark of aging. Elife *12*, e79196.
1404 https://doi.org/10.7554/eLife.79196.

1405 24. Okreglicka, K., Iten, I., Pohlmeier, L., Onder, L., Feng, Q., Kurrer, M., Ludewig, B.,
1406 Nielsen, P., Schneider, C., and Kopf, M. (2021). PPARγ is essential for the development of bone
1407 marrow erythroblastic island macrophages and splenic red pulp macrophages. J Exp Med *218*,
1408 e20191314. https://doi.org/10.1084/jem.20191314.

1409 25. Delaby, C., Pilard, N., Puy, H., and Canonne-Hergaux, F. (2008). Sequential regulation of
1410 ferroportin expression after erythrophagocytosis in murine macrophages: early mRNA induction
1411 by haem, followed by iron-dependent protein expression. Biochem J *411*, 123–131.
1412 https://doi.org/10.1042/BJ20071474.

1413 26. Bian, Z., Shi, L., Guo, Y.-L., Lv, Z., Tang, C., Niu, S., Tremblay, A., Venkataramani, M.,
1414 Culpepper, C., Li, L., et al. (2016). Cd47-Sirpα interaction and IL-10 constrain inflammation-
1415 induced macrophage phagocytosis of healthy self-cells. Proc Natl Acad Sci U S A *113*, E5434-
1416 5443. https://doi.org/10.1073/pnas.1521069113.

1417 27. Bennett, L.F., Liao, C., Quickel, M.D., Yeoh, B.S., Vijay-Kumar, M., Hankey-Giblin, P.,
1418 Prabhu, K.S., and Paulson, R.F. (2019). Inflammation induces stress erythropoiesis through heme-
1419 dependent activation of SPI-C. Sci Signal *12*, eaap7336. https://doi.org/10.1126/scisignal.aap7336.

1420 28. Ma, S., Dubin, A.E., Zhang, Y., Mousavi, S.A.R., Wang, Y., Coombs, A., Loud, M.,
1421 Andolfo, I., and Patapoutian, A. (2021). A role of PIEZO1 in iron metabolism in mice and humans.
1422 Cell *184*, 969-982.e13. https://doi.org/10.1016/j.cell.2021.01.024.

1423 29. Camaschella, C. (2019). Iron deficiency. Blood *133*, 30–39. https://doi.org/10.1182/blood-
1424 2018-05-815944.

1425 30. Pasricha, S.-R., Tye-Din, J., Muckenthaler, M.U., and Swinkels, D.W. (2021). Iron
1426 deficiency. Lancet *397*, 233–248. https://doi.org/10.1016/S0140-6736(20)32594-0.

1427 31. GBD 2021 Anaemia Collaborators (2023). Prevalence, years lived with disability, and
1428 trends in anaemia burden by severity and cause, 1990-2021: findings from the Global Burden of
1429 Disease Study 2021. Lancet Haematol *10*, e713–e734. https://doi.org/10.1016/S2352-
1430 3026(23)00160-6.

1431 32. https://www.who.int/publications/m/item/iron-children-6to23--archived-iron-deficiency-
1432 anaemia-assessment-prevention-and-control.

1433 33. Camaschella, C., and Girelli, D. (2020). The changing landscape of iron deficiency. Mol
1434 Aspects Med *75*, 100861. https://doi.org/10.1016/j.mam.2020.100861.

1435 34. Al-Naseem, A., Sallam, A., Choudhury, S., and Thachil, J. (2021). Iron deficiency without
1436 anaemia: a diagnosis that matters. Clin Med (Lond) *21*, 107–113.
1437 https://doi.org/10.7861/clinmed.2020-0582.

1438 35. Prasanth, R. (2017). Prevalence of Anemia in both Developing and Developed Countries
1439 around the World. World Journal of Anemia *1*, 40–43. https://doi.org/10.5005/jp-journals-10065-
1440 0009.

1441 36. Chaparro, C.M., and Suchdev, P.S. (2019). Anemia epidemiology, pathophysiology, and
1442 etiology in low- and middle-income countries. Ann N Y Acad Sci *1450*, 15–31.
1443 https://doi.org/10.1111/nyas.14092.

1444 37. Pasricha, S.-R., Drakesmith, H., Black, J., Hipgrave, D., and Biggs, B.-A. (2013). Control
1445 of iron deficiency anemia in low- and middle-income countries. Blood *121*, 2607–2617.
1446 https://doi.org/10.1182/blood-2012-09-453522.

1447 38. Klei, T.R.L., Dalimot, J., Nota, B., Veldthuis, M., Mul, F.P.J., Rademakers, T.,
1448 Hoogenboezem, M., Nagelkerke, S.Q., van IJcken, W.F.J., Oole, E., et al. (2020). Hemolysis in the
1449 spleen drives erythrocyte turnover. Blood *136*, 1579–1589.
1450 https://doi.org/10.1182/blood.2020005351.

1451 39. Akilesh, H.M., Buechler, M.B., Duggan, J.M., Hahn, W.O., Matta, B., Sun, X., Gessay, G.,
1452 Whalen, E., Mason, M., Presnell, S.R., et al. (2019). Chronic TLR7 and TLR9 signaling drives
1453 anemia via differentiation of specialized hemophagocytes. Science *363*, eaao5213.
1454 https://doi.org/10.1126/science.aao5213.

1455 40. Liu, Z., Gu, Y., Chakarov, S., Bleriot, C., Kwok, I., Chen, X., Shin, A., Huang, W., Dress,
1456 R.J., Dutertre, C.-A., et al. (2019). Fate Mapping via Ms4a3-Expression History Traces Monocyte-
1457 Derived Cells. Cell *178*, 1509-1525.e19. https://doi.org/10.1016/j.cell.2019.08.009.

1458 41. Palmieri, M., Impey, S., Kang, H., di Ronza, A., Pelz, C., Sardiello, M., and Ballabio, A.
1459 (2011). Characterization of the CLEAR network reveals an integrated control of cellular clearance
1460 pathways. Hum Mol Genet *20*, 3852–3866. https://doi.org/10.1093/hmg/ddr306.

1461 42. Bussi, C., and Gutierrez, M.G. (2024). One size does not fit all: Lysosomes exist in
1462 biochemically and functionally distinct states. PLoS Biol *22*, e3002576.
1463 https://doi.org/10.1371/journal.pbio.3002576.

1464 43. Rovira, M., Sereda, R., Pladevall-Morera, D., Ramponi, V., Marin, I., Maus, M., Madrigal-
1465 Matute, J., Díaz, A., García, F., Muñoz, J., et al. (2022). The lysosomal proteome of senescent cells

contributes to the senescence secretome. Aging Cell *21*, e13707. https://doi.org/10.1111/acel.13707.

44. Vinchi, F., Costa da Silva, M., Ingoglia, G., Petrillo, S., Brinkman, N., Zuercher, A., Cerwenka, A., Tolosano, E., and Muckenthaler, M.U. (2016). Hemopexin therapy reverts heme-induced proinflammatory phenotypic switching of macrophages in a mouse model of sickle cell disease. Blood *127*, 473–486. https://doi.org/10.1182/blood-2015-08-663245.

45. Pfefferlé, M., Ingoglia, G., Schaer, C.A., Yalamanoglu, A., Buzzi, R., Dubach, I.L., Tan, G., López-Cano, E.Y., Schulthess, N., Hansen, K., et al. (2020). Hemolysis transforms liver macrophages into antiinflammatory erythrophagocytes. J Clin Invest *130*, 5576–5590. https://doi.org/10.1172/JCI137282.

46. Pereira, M., Chen, T.-D., Buang, N., Olona, A., Ko, J.-H., Prendecki, M., Costa, A.S.H., Nikitopoulou, E., Tronci, L., Pusey, C.D., et al. (2019). Acute Iron Deprivation Reprograms Human Macrophage Metabolism and Reduces Inflammation In Vivo. Cell Rep *28*, 498-511.e5. https://doi.org/10.1016/j.celrep.2019.06.039.

47. Pagani, A., Nai, A., Corna, G., Bosurgi, L., Rovere-Querini, P., Camaschella, C., and Silvestri, L. (2011). Low hepcidin accounts for the proinflammatory status associated with iron deficiency. Blood *118*, 736–746. https://doi.org/10.1182/blood-2011-02-337212.

48. Diskin, C., and Pålsson-McDermott, E.M. (2018). Metabolic Modulation in Macrophage Effector Function. Front Immunol *9*, 270. https://doi.org/10.3389/fimmu.2018.00270.

49. Luo, B., Gan, W., Liu, Z., Shen, Z., Wang, J., Shi, R., Liu, Y., Liu, Y., Jiang, M., Zhang, Z., et al. (2016). Erythropoeitin Signaling in Macrophages Promotes Dying Cell Clearance and Immune Tolerance. Immunity *44*, 287–302. https://doi.org/10.1016/j.immuni.2016.01.002.

50. Finberg, K.E., Heeney, M.M., Campagna, D.R., Aydinok, Y., Pearson, H.A., Hartman, K.R., Mayo, M.M., Samuel, S.M., Strouse, J.J., Markianos, K., et al. (2008). Mutations in TMPRSS6 cause iron-refractory iron deficiency anemia (IRIDA). Nat Genet *40*, 569–571. https://doi.org/10.1038/ng.130.

51. Folgueras, A.R., de Lara, F.M., Pendás, A.M., Garabaya, C., Rodríguez, F., Astudillo, A., Bernal, T., Cabanillas, R., López-Otín, C., and Velasco, G. (2008). Membrane-bound serine protease matriptase-2 (Tmprss6) is an essential regulator of iron homeostasis. Blood *112*, 2539–2545. https://doi.org/10.1182/blood-2008-04-149773.

52. Silvestri, L., Pagani, A., Nai, A., De Domenico, I., Kaplan, J., and Camaschella, C. (2008). The serine protease matriptase-2 (TMPRSS6) inhibits hepcidin activation by cleaving membrane hemojuvelin. Cell Metab *8*, 502–511. https://doi.org/10.1016/j.cmet.2008.09.012.

53. Nai, A., Pagani, A., Mandelli, G., Lidonnici, M.R., Silvestri, L., Ferrari, G., and Camaschella, C. (2012). Deletion of TMPRSS6 attenuates the phenotype in a mouse model of β-thalassemia. Blood *119*, 5021–5029. https://doi.org/10.1182/blood-2012-01-401885.

54. Finberg, K.E., Whittlesey, R.L., Fleming, M.D., and Andrews, N.C. (2010). Down-regulation of Bmp/Smad signaling by Tmprss6 is required for maintenance of systemic iron homeostasis. Blood *115*, 3817–3826. https://doi.org/10.1182/blood-2009-05-224808.

55. Manolova, V., Nyffenegger, N., Flace, A., Altermatt, P., Varol, A., Doucerain, C., Sundstrom, H., and Dürrenberger, F. (2019). Oral ferroportin inhibitor ameliorates ineffective

1507 erythropoiesis in a model of β-thalassemia. Journal of Clinical Investigation *130*, 491–506.
1508 https://doi.org/10.1172/JCI129382.

1509 56. Sawyer, D.W., Sullivan, J.A., and Mandell, G.L. (1985). Intracellular free calcium
1510 localization in neutrophils during phagocytosis. Science *230*, 663–666.
1511 https://doi.org/10.1126/science.4048951.

1512 57. Shen, J., Wilbon, A.S., Zhou, M., and Pan, Y. (2023). Mechanism of Ca2+ transport by
1513 ferroportin. Elife *12*, e82947. https://doi.org/10.7554/eLife.82947.

1514 58. Zumerle, S., Calì, B., Munari, F., Angioni, R., Di Virgilio, F., Molon, B., and Viola, A.
1515 (2019). Intercellular Calcium Signaling Induced by ATP Potentiates Macrophage Phagocytosis.
1516 Cell Rep *27*, 1-10.e4. https://doi.org/10.1016/j.celrep.2019.03.011.

1517 59. Schilperoort, M., Ngai, D., Sukka, S.R., Avrampou, K., Shi, H., and Tabas, I. (2023). The
1518 role of efferocytosis-fueled macrophage metabolism in the resolution of inflammation. Immunol
1519 Rev *319*, 65–80. https://doi.org/10.1111/imr.13214.

1520 60. Bhutia, Y.D., and Ganapathy, V. (2016). Glutamine transporters in mammalian cells and
1521 their functions in physiology and cancer. Biochimica et Biophysica Acta (BBA) - Molecular Cell
1522 Research *1863*, 2531–2539. https://doi.org/10.1016/j.bbamcr.2015.12.017.

1523 61. Beard, J. (2003). Iron deficiency alters brain development and functioning. J Nutr *133*,
1524 1468S-72S. https://doi.org/10.1093/jn/133.5.1468S.

1525 62. Badaracco, M.E., Ortiz, E.H., Soto, E.F., Connor, J., and Pasquini, J.M. (2008). Effect of
1526 transferrin on hypomyelination induced by iron deficiency. J Neurosci Res *86*, 2663–2673.
1527 https://doi.org/10.1002/jnr.21709.

1528 63. Jiang, Y., Li, C., Wu, Q., An, P., Huang, L., Wang, J., Chen, C., Chen, X., Zhang, F., Ma,
1529 L., et al. (2019). Iron-dependent histone 3 lysine 9 demethylation controls B cell proliferation and
1530 humoral immune responses. Nat Commun *10*, 2935. https://doi.org/10.1038/s41467-019-11002-5.

1531 64. Zhu, L., Li, G., Liang, Z., Qi, T., Deng, K., Yu, J., Peng, Y., Zheng, J., Song, Y., and Chang,
1532 X. (2023). Microbiota-assisted iron uptake promotes immune tolerance in the intestine. Nat
1533 Commun *14*, 2790. https://doi.org/10.1038/s41467-023-38444-2.

1534 65. Wang, L., Johnson, E.E., Shi, H.N., Allan Walker, W., Wessling-Resnick, M., and Cherayil,
1535 B.J. (2008). Attenuated inflammatory responses in hemochromatosis reveal a role for iron in the
1536 regulation of macrophage cytokine translation. J Immunol *181*, 2723–2731.

1537 66. Agoro, R., Taleb, M., Quesniaux, V.F.J., and Mura, C. (2018). Cell iron status influences
1538 macrophage polarization. PLoS One *13*, e0196921. https://doi.org/10.1371/journal.pone.0196921.

1539 67. Mleczko-Sanecka, K., and Silvestri, L. (2021). Cell-type-specific insights into iron
1540 regulatory processes. Am J Hematol *96*, 110–127. https://doi.org/10.1002/ajh.26001.

1541 68. Xu, W., Barrientos, T., Mao, L., Rockman, H.A., Sauve, A.A., and Andrews, N.C. (2015).
1542 Lethal Cardiomyopathy in Mice Lacking Transferrin Receptor in the Heart. Cell Rep *13*, 533–545.
1543 https://doi.org/10.1016/j.celrep.2015.09.023.

1544 69. Papathanassiu, A.E., Ko, J.-H., Imprialou, M., Bagnati, M., Srivastava, P.K., Vu, H.A.,
1545 Cucchi, D., McAdoo, S.P., Ananieva, E.A., Mauro, C., et al. (2017). BCAT1 controls metabolic
1546 reprogramming in activated human macrophages and is associated with inflammatory diseases. Nat

1547 Commun *8*, 16040. https://doi.org/10.1038/ncomms16040.

1548 70. Lu, M., Luo, D., Zhang, Z., Ouyang, F., Shi, Y., Hu, C., Su, H., Li, Y., Zhang, J., Gui, Q.,
1549 et al. (2024). Branched-chain amino acid catabolism promotes M2 macrophage polarization. Front.
1550 Immunol. *15*, 1469163. https://doi.org/10.3389/fimmu.2024.1469163.

1551 71. Yan, H., Liu, Y., Li, X., Yu, B., He, J., Mao, X., Yu, J., Huang, Z., Luo, Y., Luo, J., et al.
1552 (2024). Leucine alleviates cytokine storm syndrome by regulating macrophage polarization via the
1553 mTORC1/LXRα signaling pathway. eLife *12*, RP89750. https://doi.org/10.7554/eLife.89750.

1554 72. Banerjee, S., Lu, S., Jain, A., Wang, I., Tao, H., Srinivasan, S., Nemeth, E., and He, P.
1555 (2024). Targeting PKCa alleviates iron overload in diabetes and hemochromatosis through the
1556 inhibition of ferroportin. Blood, blood.2024023829. https://doi.org/10.1182/blood.2024023829.

1557 73. Ennerfelt, H., Frost, E.L., Shapiro, D.A., Holliday, C., Zengeler, K.E., Voithofer, G., Bolte,
1558 A.C., Lammert, C.R., Kulas, J.A., Ulland, T.K., et al. (2022). SYK coordinates neuroprotective
1559 microglial responses in neurodegenerative disease. Cell *185*, 4135-4152.e22.
1560 https://doi.org/10.1016/j.cell.2022.09.030.

1561 74. Wang, S., Sudan, R., Peng, V., Zhou, Y., Du, S., Yuede, C.M., Lei, T., Hou, J., Cai, Z.,
1562 Cella, M., et al. (2022). TREM2 drives microglia response to amyloid-β via SYK-dependent and -
1563 independent pathways. Cell *185*, 4153-4169.e19. https://doi.org/10.1016/j.cell.2022.09.033.

1564 75. Kobayashi, A., Azuma, K., Takeiwa, T., Kitami, T., Horie, K., Ikeda, K., and Inoue, S.
1565 (2023). A FRET-based respirasome assembly screen identifies spleen tyrosine kinase as a target to
1566 improve muscle mitochondrial respiration and exercise performance in mice. Nat Commun *14*,
1567 312. https://doi.org/10.1038/s41467-023-35865-x.

1568 76. Canton, J., Khezri, R., Glogauer, M., and Grinstein, S. (2014). Contrasting phagosome pH
1569 regulation and maturation in human M1 and M2 macrophages. Mol Biol Cell *25*, 3330–3341.
1570 https://doi.org/10.1091/mbc.E14-05-0967.

1571 77. Das Gupta, K., Shakespear, M.R., Curson, J.E.B., Murthy, A.M.V., Iyer, A., Hodson, M.P.,
1572 Ramnath, D., Tillu, V.A., von Pein, J.B., Reid, R.C., et al. (2020). Class IIa Histone Deacetylases
1573 Drive Toll-like Receptor-Inducible Glycolysis and Macrophage Inflammatory Responses via
1574 Pyruvate Kinase M2. Cell Rep *30*, 2712-2728.e8. https://doi.org/10.1016/j.celrep.2020.02.007.

1575 78. Codo, A.C., Davanzo, G.G., Monteiro, L. de B., de Souza, G.F., Muraro, S.P., Virgilio-da-
1576 Silva, J.V., Prodonoff, J.S., Carregari, V.C., de Biagi Junior, C.A.O., Crunfli, F., et al. (2020).
1577 Elevated Glucose Levels Favor SARS-CoV-2 Infection and Monocyte Response through a HIF-
1578 1α/Glycolysis-Dependent Axis. Cell Metab *32*, 437-446.e5.
1579 https://doi.org/10.1016/j.cmet.2020.07.007.

1580 79. Van den Bossche, J., O'Neill, L.A., and Menon, D. (2017). Macrophage
1581 Immunometabolism: Where Are We (Going)? Trends Immunol *38*, 395–406.
1582 https://doi.org/10.1016/j.it.2017.03.001.

1583 80. Divakaruni, A.S., Hsieh, W.Y., Minarrieta, L., Duong, T.N., Kim, K.K.O., Desousa, B.R.,
1584 Andreyev, A.Y., Bowman, C.E., Caradonna, K., Dranka, B.P., et al. (2018). Etomoxir Inhibits
1585 Macrophage Polarization by Disrupting CoA Homeostasis. Cell Metab *28*, 490-503.e7.
1586 https://doi.org/10.1016/j.cmet.2018.06.001.

1587 81. Liu, P.-S., Wang, H., Li, X., Chao, T., Teav, T., Christen, S., Di Conza, G., Cheng, W.-C.,

1588 Chou, C.-H., Vavakova, M., et al. (2017). α-ketoglutarate orchestrates macrophage activation
1589 through metabolic and epigenetic reprogramming. Nat Immunol *18*, 985–994.
1590 https://doi.org/10.1038/ni.3796.

1591 82. Mills, E.L., Kelly, B., Logan, A., Costa, A.S.H., Varma, M., Bryant, C.E., Tourlomousis,
1592 P., Däbritz, J.H.M., Gottlieb, E., Latorre, I., et al. (2016). Succinate Dehydrogenase Supports
1593 Metabolic Repurposing of Mitochondria to Drive Inflammatory Macrophages. Cell *167*, 457-
1594 470.e13. https://doi.org/10.1016/j.cell.2016.08.064.

1595 83. Torrance, J.D., and Bothwell, T.H. (1968). A simple technique for measuring storage iron
1596 concentrations in formalinised liver samples. S Afr J Med Sci *33*, 9–11.

1597 84. Moggridge, S., Sorensen, P.H., Morin, G.B., and Hughes, C.S. (2018). Extending the
1598 Compatibility of the SP3 Paramagnetic Bead Processing Approach for Proteomics. J Proteome Res
1599 *17*, 1730–1740. https://doi.org/10.1021/acs.jproteome.7b00913.

1600 85. Hughes, C.S., Foehr, S., Garfield, D.A., Furlong, E.E., Steinmetz, L.M., and Krijgsveld, J.
1601 (2014). Ultrasensitive proteome analysis using paramagnetic bead technology. Mol Syst Biol *10*,
1602 757. https://doi.org/10.15252/msb.20145625.

1603 86. Werner, T., Sweetman, G., Savitski, M.F., Mathieson, T., Bantscheff, M., and Savitski,
1604 M.M. (2014). Ion coalescence of neutron encoded TMT 10-plex reporter ions. Anal Chem *86*,
1605 3594–3601. https://doi.org/10.1021/ac500140s.

1606 87. Yang, F., Shen, Y., Camp, D.G., and Smith, R.D. (2012). High-pH reversed-phase
1607 chromatography with fraction concatenation for 2D proteomic analysis. Expert Rev Proteomics *9*,
1608 129–134. https://doi.org/10.1586/epr.12.15.

1609